

PAPER • OPEN ACCESS

Imaging nuclear shape through anisotropic and radial flow in high-energy heavy-ion collisions

To cite this article: The STAR Collaboration 2025 *Rep. Prog. Phys.* **88** 108601

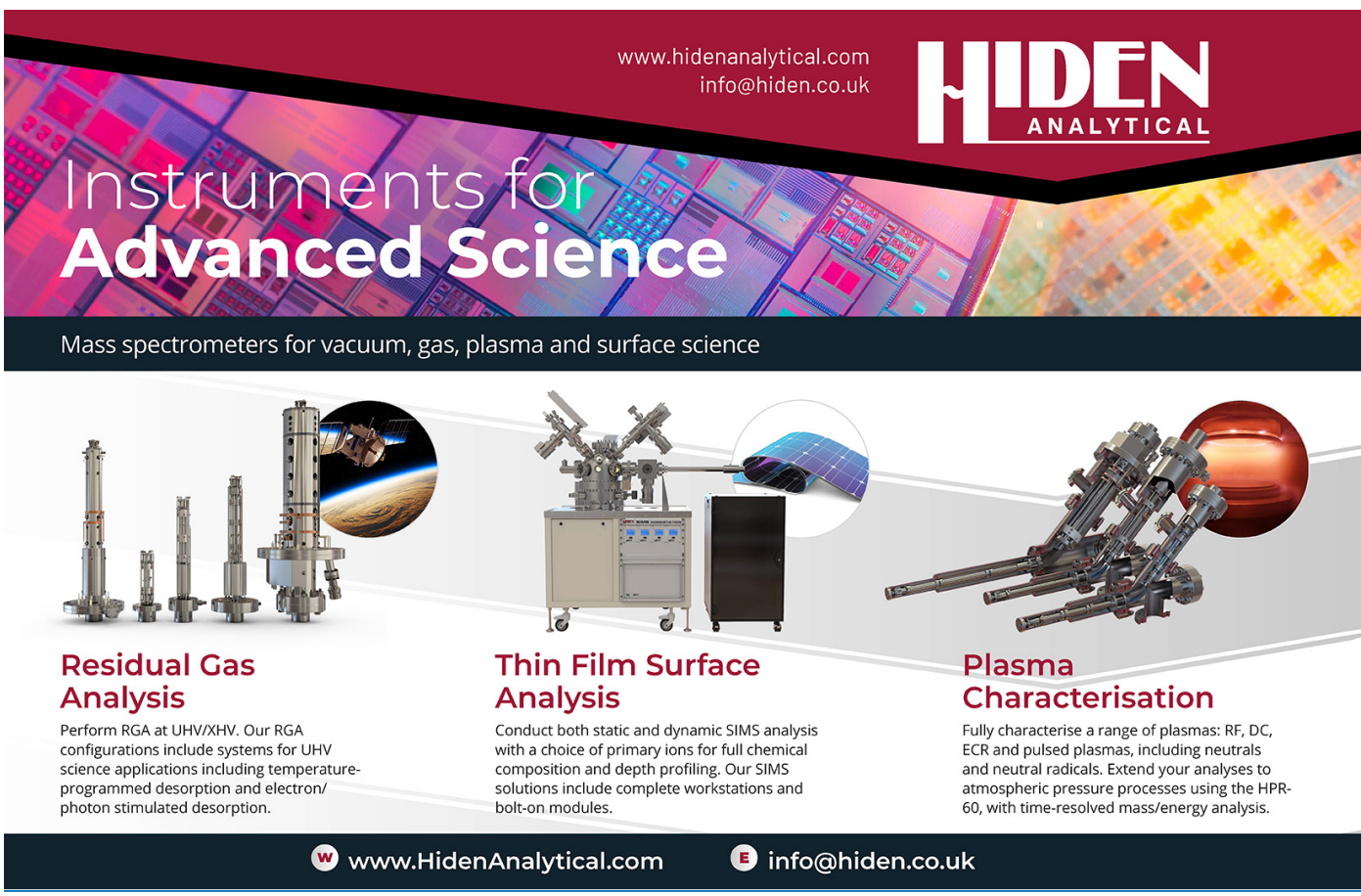
View the [article online](#) for updates and enhancements.

You may also like

- [Disentangling the Cosmic Web toward FRB 190608](#)
Sunil Simha, Joseph N. Burchett, J. Xavier Prochaska et al.

- [Reconstruction from boundary measurements for less regular conductivities](#)
Andoni Garcia and Guo Zhang

- [Impact of Se and Te addition on optical characteristics of ternary GeInSb chalcogenide films as promising materials for optoelectronic applications](#)
E G El-Metwally, H E Atyia and A M Ismail



www.hidenanalytical.com
info@hiden.co.uk

HIDEN ANALYTICAL

Instruments for Advanced Science

Mass spectrometers for vacuum, gas, plasma and surface science

Residual Gas Analysis

Perform RGA at UHV/XHV. Our RGA configurations include systems for UHV science applications including temperature-programmed desorption and electron/photon stimulated desorption.

Thin Film Surface Analysis

Conduct both static and dynamic SIMS analysis with a choice of primary ions for full chemical composition and depth profiling. Our SIMS solutions include complete workstations and bolt-on modules.

Plasma Characterisation

Fully characterise a range of plasmas: RF, DC, ECR and pulsed plasmas, including neutrals and neutral radicals. Extend your analyses to atmospheric pressure processes using the HPR-60, with time-resolved mass/energy analysis.

 www.HidenAnalytical.com  info@hiden.co.uk

Imaging nuclear shape through anisotropic and radial flow in high-energy heavy-ion collisions

The STAR Collaboration

E-mail: star-publication@bnl.gov

Received 22 June 2025, revised 19 August 2025

Accepted for publication 6 October 2025

Published 22 October 2025

Corresponding editor: Dr Paul Mabey



Abstract

Most atomic nuclei exhibit ellipsoidal shapes characterized by quadrupole deformation β_2 and triaxiality γ , and sometimes even a pear-like octupole deformation β_3 . The STAR experiment introduced a new ‘imaging-by-smashing’ technique ((STAR Collaboration) 2024 *Nature* **635** 67; Jia 2025 *Rep. Prog. Phys.* **88** 092301) to image the nuclear global shape by colliding nuclei at ultra-relativistic speeds and analyzing outgoing debris. Features of nuclear shape manifest in collective observables like anisotropic flow v_n and radial flow via mean transverse momentum [p_T]. We present new measurements of the variances of v_n ($n = 2, 3$, and 4) and [p_T], and the covariance of v_n^2 with [p_T], in collisions of highly deformed ^{238}U and nearly spherical ^{197}Au . Ratios of these observables between the two systems effectively suppress common final-state effects, isolating the strong impact of uranium’s deformation. By comparing results with state-of-the-art hydrodynamic model calculations, we extract $\beta_{2\text{U}}$ and γ_{U} values consistent with those deduced from low-energy nuclear structure measurements. Measurements of v_3 and its correlation with [p_T] also provide the first experimental suggestion of a possible octupole deformation for ^{238}U . These findings provide significant support for using high-energy collisions to explore nuclear shapes on femtosecond timescales, with implications for both nuclear structure and quark-gluon plasma studies.

Keywords: quark-gluon plasma, nuclear structure, anisotropic flow, nuclear shape, quadrupole deformation, octupole deformation, imaging-by-smashing

Contents

1. Introduction	2	3. Results	7
2. Analysis	4	3.1. General trends and the signatures of deformation	7
2.1. Event and track selections	4	3.2. Dependence on correlation methods and kinematic selections	9
2.2. Calculation of observables	4	3.3. Ratios between the two systems	10
2.3. Influence of non-flow correlations	6	4. Model comparisons	12
2.4. Systematic uncertainties	6	4.1. Comparisons with initial-state and hydrodynamic models for v_n – p_T correlations	12
		4.2. Quantitative constraints on Uranium deformation parameters	16
		5. Summary and outlook	19
		Data availability statement	21
		Acknowledgments	22
		Appendix. Comprehensive data plots	22
		References	27



Original Content from this work may be used under the terms of the [Creative Commons Attribution 4.0 licence](#). Any further distribution of this work must maintain attribution to the author(s) and the title of the work, journal citation and DOI.

1. Introduction

High-energy heavy-ion collisions, conducted at the relativistic heavy ion collider (RHIC) and the large Hadron collider (LHC), have been used to produce and study the quark-gluon plasma (QGP). This deconfined state of matter undergoes a spacetime evolution that is well-described by relativistic hydrodynamics [1]. The hydrodynamic expansion translates initial spatial anisotropies and size variations within the QGP into measurable patterns in the azimuthal and radial distributions of outgoing particles in the momentum space, observed as anisotropic [2, 3] and radial flow [4, 5], respectively. While these observables contain vital information about the transport properties of the QGP, their interpretation is complicated by inherent uncertainties in the initial conditions—the spatial distribution of energy density before the hydrodynamic evolution. The initial conditions cannot be calculated directly from first principles; they must be inferred alongside QGP properties using hydrodynamic models, which introduces significant uncertainties in both [6–8]. Consequently, it is important to develop methods to disentangle the influence of initial conditions from final-state effects.

Initial condition and nuclear shape. The connection between the initial conditions and observed final-state flow is relatively well-established [1]. The initial geometry of the collision, characterized by eccentricities ε_n ($n = 2, 3, 4, \dots$), directly drives the azimuthal anisotropies in the particle distribution, described by $dN/d\phi \propto 1 + 2 \sum v_n \cos(n\phi)$, where v_2 , v_3 , and v_4 represent the dominant elliptic, triangular, and quadrangular flow components [9, 10], respectively. Similarly, the compactness of the initial conditions, quantified by the inverse area d_{\perp} of the overlap region [11], influences radial flow, as reflected in the event-by-event average transverse momentum ($\langle p_T \rangle$). Hydrodynamic models predict approximately linear relationships: $v_n \propto \varepsilon_n$ for $n = 2$ and 3 (and for $n = 4$ in central collisions) [12], and $\delta p_T \propto \delta d_{\perp}$ [13], where $\delta p_T = [p_T] - \langle [p_T] \rangle$ and $\delta d_{\perp} = d_{\perp} - \langle d_{\perp} \rangle$ represent deviations from their mean values. However, accurately describing the initial conditions requires a good understanding of both the nucleon spatial distribution within colliding nuclei and the mechanisms of energy deposition [14].

A major challenge in this endeavor arises from the fact that most atomic nuclei are deformed. Collisions of randomly oriented deformed nuclei significantly enhance event-by-event variations in both the initial size and shape of the QGP [15]. This, in turn, increases fluctuations in anisotropic and radial flow, an effect clearly demonstrated in central $^{238}\text{U}+^{238}\text{U}$ collisions by our previous measurement [16].

One powerful approach to constrain these initial conditions is to compare collision systems with similar sizes but distinct nuclear structures, such as isobar collisions [17] or, as in this study, isobar-like collisions of $^{238}\text{U}+^{238}\text{U}$ and $^{197}\text{Au}+^{197}\text{Au}$. Uranium is known to be strongly prolate deformed, while gold exhibits mild oblate deformation. Despite these shape differences, the resulting QGPs are of comparable sizes, and the

20% difference in mass number (A) has a small impact on QGP properties [18]. Consequently, ratios of bulk observables between these two systems largely cancel common final-state effects, thereby isolating variations in the initial conditions that stem from the structural differences between ^{238}U and ^{197}Au [19, 20]. Analyzing these ratios as a function of nuclear shape also provides valuable insights into the energy deposition mechanisms [21].

Nuclear shape, including the dominant quadrupole component β_2 , and smaller axial octupole β_3 and axial hexadecapole β_4 components, can be described by a Woods-Saxon density profile,

$$\rho(r, \theta, \phi) \propto (1 + \exp[r - R(\theta, \phi)/a])^{-1}, \\ R(\theta, \phi) = R_0(1 + \beta_2[\cos \gamma Y_{2,0} + \sin \gamma Y_{2,2}] + \beta_3 Y_{3,0} + \beta_4 Y_{4,0}), \quad (1)$$

where $R_0 = 1.2A^{1/3}$ is the nuclear radius, a is the surface or skin depth, and $Y_{l,m}(\theta, \phi)$ are real spherical harmonics in the intrinsic frame. The triaxiality parameter γ (ranging from 0° to 60°) determines the relative ordering of the three principal radii (r_a, r_b, r_c). Specifically, $\gamma = 0^\circ$ corresponds to a prolate shape ($r_a = r_b < r_c$), $\gamma = 60^\circ$ to an oblate shape ($r_a < r_b = r_c$), and intermediate values to a triaxial shape ($r_a < r_b < r_c$).

Manifestation of nuclear shapes from low to high energies. Traditionally, nuclear shapes are inferred from spectroscopic or scattering experiments conducted at sub-hundred MeV/nucleon beam energies [22–24], which probe collective nuclear shapes on timescales longer than 100 fm c^{-1} . For instance, the ^{238}U nucleus, with an even number of protons and neutrons, exhibits a rotational spectrum consistent with a prolate rigid rotor. Estimates based on electric quadrupole transition data and rigid rotor assumption yield $\beta_{2\text{U}} = 0.287 \pm 0.007$ [25] and $\gamma_{\text{U}} \lesssim 8^\circ$ [26]. Direct measurements of $\beta_{3\text{U}}$ and $\beta_{4\text{U}}$ are lacking, but model-dependent estimates suggest values around $\beta_{3\text{U}} \sim 0.08$ and $\beta_{4\text{U}} \sim 0.1$ [27, 28]. The shape of the odd-mass ^{197}Au nucleus is less certain, with low-energy model calculations suggesting $\beta_{2\text{Au}} = 0.1\text{--}0.14$ and $\gamma_{\text{Au}} \sim 45^\circ$ [29, 30].

The quantum mechanical nature of nuclear ground states deserves careful consideration in this context. It is understood that the wavefunction of a ground state nucleus is a superposition of all possible orientations, and its shape is not directly observable if nucleus stays in its ground state [22]. However, high-energy heavy-ion collisions are strongly interacting, dynamical systems, for which the stationary solution of an individual nucleus is not an eigenstate of the combined two-nuclei system. Instead, the extremely fast smashing process ($\lesssim 0.1 \text{ fm c}^{-1}$, corresponding to the crossing time of colliding nuclei) acts as a quantum measurement that projects nucleons into their position space, from which a shape and orientation can be defined.

Furthermore, high-energy heavy-ion collisions are sensitive not only to these global nuclear shapes relevant at

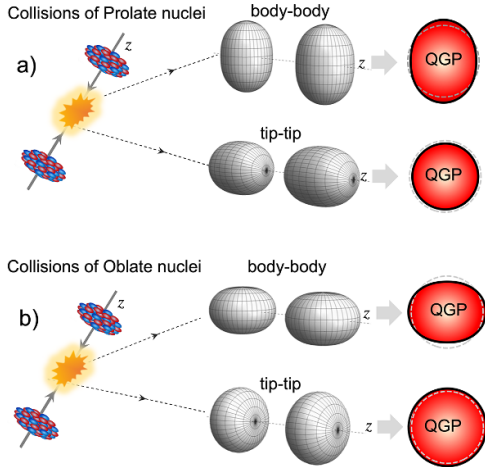


Figure 1. Illustration of how collision geometry and collective expansion are impacted by quadrupole deformation in collisions of prolate (a) and oblate (b) nuclei. The configurations vary between body–body and tip–tip, which are selected based on the momentum distribution of final state particles. The negative (positive) correlation between ellipticity and inverse size in (a) ((b)) drives the negative (positive) correlation between elliptic flow and radial flow in the final state, highlighting the potential of constraining the triaxiality. The dashed gray circles represent the baseline shape of the QGP for spherical nuclei.

low-energy, but also to fluctuations of the nuclear wavefunction on much shorter timescales. This makes high-energy collisions a novel tool for investigating nuclear structure and its evolution with energy [31].

Nuclear deformation influences high-energy collisions by modifying the nucleon distribution in the overlap region and, consequently, the initial conditions of the QGP. In collisions of prolate nuclei (figure 1(a)), the initial configuration varies between body–body (high ε_2 , low d_{\perp}) and tip–tip (low ε_2 , high d_{\perp}) collisions. This leads to enhanced, anti-correlated event-by-event fluctuations in ε_2 and d_{\perp} [32]. Collisions of oblate nuclei also exhibit enhanced fluctuations, but with a positive correlation between ε_2 and d_{\perp} (figure 1(b)). These effects are quantitatively captured by the moments of the ε_2 and d_{\perp} distributions, including the variances $\langle \varepsilon_2^2 \rangle$ and $\langle (\delta d_{\perp})^2 \rangle$, and the skewness $\langle \varepsilon_2^2 \delta d_{\perp} \rangle$. Here, the angle brackets ' $\langle \cdot \rangle$ ' denote averages over events within a given centrality class. Similarly, the presence of modest higher-order deformations β_3 and β_4 is expected to slightly enhance the fluctuations of ε_3 and ε_4 , respectively [15].

Extraction of nuclear shape in high-energy collisions. Our analysis focuses on the moments of the final-state flow observables: $\langle v_2^2 \rangle$, $\langle (\delta p_T)^2 \rangle$, and $\langle v_2^2 \delta p_T \rangle$ [33]. These observables are sensitive to quadrupole deformation due to their approximately linear relationships with $\langle \varepsilon_2^2 \rangle$, $\langle (\delta d_{\perp})^2 \rangle$, and $\langle \varepsilon_2^2 \delta d_{\perp} \rangle$. For small deformations and using a Taylor expansion, one can show that these quantities follow simple parametric dependencies on the shape parameters [34]:

$$\begin{aligned} \langle v_2^2 \rangle &= a_1 + b_1 \beta_2^2, \\ \langle (\delta p_T)^2 \rangle &= a_2 + b_2 \beta_2^2, \\ \langle v_2^2 \delta p_T \rangle &= a_3 - b_3 \beta_2^3 \cos(3\gamma), \end{aligned} \quad (2)$$

where the positive coefficients a_n and b_n depend on the collision geometry and QGP properties. The b_n values are nearly independent of centrality, while the a_n values are minimized in central collisions, making central collisions ideal for constraining nuclear shape. The $\cos(3\gamma)$ term distinguishes between prolate and oblate nuclei, as expected from figure 1. We also measure correlators involving high-order flow coefficients: $\langle v_3^2 \rangle$, $\langle v_4^2 \rangle$, $\langle v_3^2 \delta p_T \rangle$ and $\langle v_4^2 \delta p_T \rangle$. These observables are expected to be minimally sensitive to β_2 and γ [15, 35], thus serving as crucial control measurements. Conversely, they are sensitive to high-order deformations β_3 and β_4 , potentially enabling searches for the presence of these deformations in ^{238}U [36]. For example, observables involving v_3 are sensitive to octupole deformation:

$$\begin{aligned} \langle v_3^2 \rangle &= a_3 + b_3 \beta_2^2, \\ \langle v_3^2 \delta p_T \rangle &= a_4 - b_4 \beta_2 \beta_3^2. \end{aligned} \quad (3)$$

We employ two complementary approaches to probe the initial conditions and quantify the effects of nuclear deformation. The primary approach utilizes ratios of flow observables between U+U and Au+Au collisions:

$$R_{\mathcal{O}} = \frac{\langle \mathcal{O} \rangle_{\text{U}}}{\langle \mathcal{O} \rangle_{\text{Au}}}, \quad \langle \mathcal{O} \rangle = \langle v_n^2 \rangle, \langle (\delta p_T)^2 \rangle, \text{ or } \langle v_n^2 \delta p_T \rangle. \quad (4)$$

The deformation of uranium is expected to cause these ratios to deviate significantly from unity, particularly in central collisions. The second approach constructs normalized quantities involving the three observables within a single collision system:

$$\rho_n^{\text{pcc}} \equiv \frac{\langle v_n^2 \delta p_T \rangle}{\sqrt{\text{var}(v_n^2)} \sqrt{\langle (\delta p_T)^2 \rangle}}, \quad (5)$$

$$\rho_n \equiv \frac{\langle v_n^2 \delta p_T \rangle}{\langle v_n^2 \rangle \sqrt{\langle (\delta p_T)^2 \rangle}}. \quad (6)$$

Here, $\text{var}(v_n^2) = \langle v_n^4 \rangle - \langle v_n^2 \rangle^2$ is the variance of v_n^2 . The observable ρ_n^{pcc} is the Pearson correlation coefficient [33], while ρ_n , introduced in [34], better captures the spherical baseline. Both observables are expected to be strongly modified in U+U ultra-central collisions (UCCs) for $n=2$, but not for $n=3$ and 4. These normalized observables are also sensitive to other aspects of the initial conditions, including nucleon width [37], initial momentum anisotropy [38], and sub-leading radial structure [11].

The influence of β_2 on v_2 was recognized in early studies [39–43], and confirmed by experiments at RHIC [44] and the LHC [45–47]. Recently, the STAR collaboration observed

enhanced $\langle (\delta p_T)^2 \rangle$ and a clear negative $\langle v_2^2 \delta p_T \rangle$ signal in central $^{238}\text{U} + ^{238}\text{U}$ collisions [16]. The strength of $\langle v_2^2 \delta p_T \rangle$ is much stronger than the correlation between v_2 and total multiplicity previously explored [44]. By analyzing ratios (equation (4)) between $^{238}\text{U} + ^{238}\text{U}$ and $^{197}\text{Au} + ^{197}\text{Au}$ collisions and comparing them with hydrodynamic model calculations, STAR have extracted $\beta_{2\text{U}}$ and γ_{U} values consistent with low-energy measurements. A similar extraction was also accomplished using a different hydrodynamic model framework [48, 49]. However, no experimental attempt has yet been made to extract β_3 and β_4 deformations.

Scope of this paper. Building on these findings, this paper presents a comprehensive study of anisotropic flow and its correlations with $[p_T]$ in $^{238}\text{U} + ^{238}\text{U}$ collisions at $\sqrt{s_{\text{NN}}} = 193$ GeV and $^{197}\text{Au} + ^{197}\text{Au}$ collisions at $\sqrt{s_{\text{NN}}} = 200$ GeV. This study extends previous results in several key aspects:

- **Normalized observables:** we compute Pearson correlation coefficients ρ_2^{pcc} and ρ_n (equations (5) and (6)), which aim to isolate deformation-driven signals by partially canceling final-state effects in a single collision system.
- **Searching for higher-order deformations:** measurements of $\langle v_3^2 \rangle$, $\langle v_4^2 \rangle$, $\langle v_3^2 \delta p_T \rangle$, and $\langle v_4^2 \delta p_T \rangle$ provide critical baselines, as these observables are largely insensitive to β_2 and γ . These observables could potentially provide evidence for the presence of modest β_3 and β_4 in ^{238}U .
- **Differential measurements:** by varying p_T ranges and pseudorapidity (η) selections, we assess the robustness of deformation signatures against non-flow correlations and sub-leading fluctuations in the initial geometry.
- **New ratio observables:** we combine $\langle v_2^2 \rangle$, $\langle (\delta p_T)^2 \rangle$, and $\langle v_2^2 \delta p_T \rangle$ after taking the difference between the two collision systems. This approach is designed to better eliminate spherical baseline terms (a_n in equation (2)), thereby enhancing sensitivity to nuclear deformation.
- **Model comparison:** we perform detailed hydrodynamic model and Glauber model calculations to extract $\beta_{2\text{U}}$ and γ_{U} , validating the ‘imaging-by-smashing’ approach against low-energy nuclear structure data.

This study demonstrates high-energy collisions as a promising imaging tool for nuclear structure research, while also advancing our understanding of the initial conditions of the QGP.

2. Analysis

2.1. Event and track selections

This analysis utilizes Au+Au collisions at $\sqrt{s_{\text{NN}}} = 200$ GeV (2010 and 2011) and U+U collisions at $\sqrt{s_{\text{NN}}} = 193$ GeV (2012), recorded by the STAR detector. Charged particles were reconstructed within $|\eta| < 1$ using the STAR time projection chamber (TPC) [50]. Minimum-bias events were selected by requiring coincident signals in the two vertex position detectors in the forward regions ($4.4 < |\eta| < 4.9$) [51]. To

enhance statistics for central collisions, special triggers requiring large TPC multiplicities and minimal activity in the zero-degree calorimeters [52] were employed.

Offline event selection required a primary vertex z_{vtx} within 30 cm of the TPC center along the beam axis and within 2 cm of the beam spot in the transverse plane. Pileup events (those containing more than one collision) and background events were reduced by selecting on the correlation between the number of TPC tracks and the number of tracks matched to the time of flight (TOF) detector [53, 54]. One type of pileup event consists of a primary event and another central event that reduces TPC reconstruction efficiency. These low-efficiency events were rejected based on the number of TPC tracks and those matched to the primary collision vertex. After these selections, the dataset comprises approximately 528 million minimum-bias (370 million from 2011) and 120 million triggered central Au+Au events, as well as approximately 300 million minimum-bias and 5 million triggered central U+U events.

Charged particle tracks included in this analysis are required to be within $0.2 < p_T < 3.0$ GeV c $^{-1}$ and $|\eta| < 1$. Standard STAR track quality criteria were applied [16]. To minimize contributions from secondary decays, the distance of closest approach (DCA) of each track to the primary vertex was required to be less than 3 cm. Tracking efficiencies in the TPC, ϵ_{TPC} , were evaluated using the standard STAR embedding technique [55]. For $p_T > 0.5$ GeV c $^{-1}$, efficiency is nearly p_T -independent, ranging from 0.72 (0.69) in the most central Au+Au (U+U) collisions to 0.92 in the most peripheral collisions. The largest p_T -dependent variation ($\sim 10\%$ of the plateau value) occurs at $0.2 < p_T < 0.5$ GeV c $^{-1}$.

Collision centrality was determined using $N_{\text{ch}}^{\text{rec}}$, the number of reconstructed tracks in $|\eta| < 0.5$ with $p_T > 0.15$ GeV c $^{-1}$. The $N_{\text{ch}}^{\text{rec}}$ distribution, corrected for vertex position and luminosity dependence, was compared to a Monte Carlo Glauber calculation to define centrality intervals as percentages of the total nucleus-nucleus inelastic cross-section [56]. An efficiency-corrected multiplicity, N_{ch} , was also computed by summing track weights for tracks with $p_T > 0.2$ GeV c $^{-1}$ and $|\eta| < 0.5$ (detailed in section 2.2).

Figure 2 shows the distributions of $N_{\text{ch}}^{\text{rec}}$ and N_{ch} for both systems. The distribution for U+U spans a wider range than Au+Au due to uranium’s larger mass and deformation. Figure 3 summarizes the mapping between $N_{\text{ch}}^{\text{rec}}$ and centrality, and between $N_{\text{ch}}^{\text{rec}}$ and N_{ch} . These mappings allow us to present the results in terms of centrality, $N_{\text{ch}}^{\text{rec}}$, or N_{ch} . Most results are presented as a function of centrality in 0%–60% centrality range, with N_{ch} dependence results included in the appendix.

2.2. Calculation of observables

The observables v_n ($n = 2, 3$, and 4), $\delta p_T = [p_T] - \langle [p_T] \rangle$, $\langle v_n^2 \delta p_T \rangle$, and other related observables are calculated using

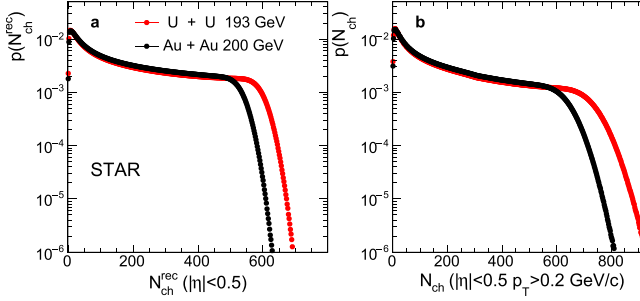


Figure 2. Distributions of reconstructed TPC track multiplicity (N_{ch}^{rec}) in $|\eta| < 0.5$ and $p_T > 0.15 \text{ GeV c}^{-1}$ (left), and efficiency-corrected TPC track multiplicity (N_{ch}) for $|\eta| < 0.5$ and $p_T > 0.2 \text{ GeV c}^{-1}$ (right), in U+U and Au+Au collisions.

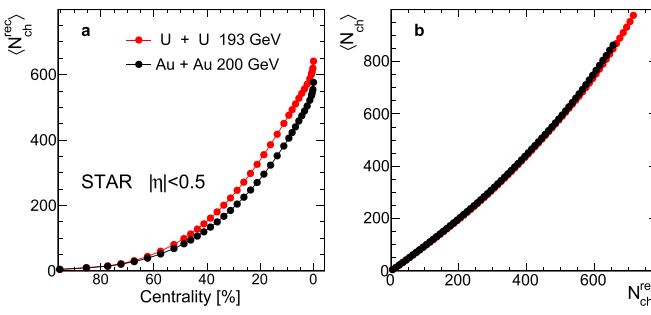


Figure 3. Relationship between centrality and N_{ch}^{rec} (left), and mapping between N_{ch}^{rec} and N_{ch} (right) in U+U and Au+Au collisions.

charged tracks as:

$$\begin{aligned} [p_T] &= \frac{\sum_i w_i p_{T,i}}{\sum_i w_i}, \langle p_T \rangle \equiv \langle [p_T] \rangle_{\text{evt}} \\ \langle (\delta p_T)^2 \rangle &= \left\langle \frac{\sum_{i \neq j} w_i w_j (p_{T,i} - \langle p_T \rangle)(p_{T,j} - \langle p_T \rangle)}{\sum_{i \neq j} w_i w_j} \right\rangle_{\text{evt}} \\ \langle v_n^2 \rangle &= \left\langle \frac{\sum_{i \neq j} w_i w_j \cos(n(\phi_i - \phi_j))}{\sum_{i \neq j} w_i w_j} \right\rangle_{\text{evt}} \\ \langle v_n^2 \delta p_T \rangle &= \left\langle \frac{\sum_{i \neq j \neq k} w_i w_j w_k \cos(n(\phi_i - \phi_j))(p_{T,k} - \langle p_T \rangle)}{\sum_{i \neq j \neq k} w_i w_j w_k} \right\rangle_{\text{evt}}. \end{aligned} \quad (7)$$

Averages are performed first over all multiplets in a single event and then over all events within a fixed N_{ch}^{rec} bin. Track-wise weights $w_{i,j,k}$ account for tracking efficiency and its ϕ -dependent variation: $w = 1/[\epsilon_{\text{TPC}} \times \text{acc}_\eta(\phi)]$. The normalized azimuthal track distribution, $\text{acc}_\eta(\phi)$, is obtained by averaging over many events in each centrality bin as a function of η . The efficiency-corrected charged particle multiplicity, N_{ch} , is calculated as $N_{ch} = \sum_i w_i$ using all reconstructed tracks within $p_T > 0.2 \text{ GeV c}^{-1}$ and $|\eta| < 0.5$.

Observables $\langle v_n^2 \rangle$ and $\langle (\delta p_T)^2 \rangle$ are obtained using both the standard method (particles i and j from $|\eta| < 1$) and the two-subevent method (particles i and j from $-1 < \eta_i < -0.1$ and $0.1 < \eta_j < 1$, respectively). The rapidity gap (on average 1.1

unit) in the two-subevent method suppresses short-range non-flow correlations from resonance decays and jets.

The covariance $\langle v_n^2 \delta p_T \rangle$ is calculated by averaging over all triplets (i , j , and k). To assess the influence of non-flow, $\langle v_n^2 \delta p_T \rangle$ is also calculated using two- and three-subevent methods [57–60]. In the two-subevent method, particles i and j are taken from $-1 < \eta_i < -0.1$ and $0.1 < \eta_j < 1$, while particle k can be taken from either subevent. In the three-subevent method, particles i , j and k are taken from distinct η ranges: $-1 < \eta_i < -0.4$, $0.4 < \eta_j < 1$, and $|\eta_k| < 0.3$. Comparing these methods quantifies the impact of non-flow correlations and longitudinal fluctuations.

The Pearson correlation coefficient ρ_n^{pcc} [33] quantifies correlations between v_n^2 and $[p_T]$ (equation (5)). The variance, $\text{var}(v_n^2)$, is obtained from the standard two- and four-particle cumulants: $c_n\{2\} = \langle v_n^2 \rangle$ and $c_n\{4\} = \langle v_n^4 \rangle - 2\langle v_n^2 \rangle^2$ [61] as [60],

$$\text{var}(v_n^2) \equiv c_n\{2\}_{\text{two-sub}}^2 + c_n\{4\}_{\text{standard}}. \quad (8)$$

Observable $c_n\{4\}$, a four-particle cumulant, is insensitive to non-flow but has poor statistical precision. Therefore, it is obtained from the standard method in the full event. The two-particle cumulants, $c_n\{2\}$, more susceptible to non-flow, are calculated using the two-subevent method.

Quadrupole deformation also influences $c_2\{4\}$:

$$c_2\{4\} = -c_1 - d_1 \beta_2^4. \quad (9)$$

where c_1 and d_1 are positive, centrality-dependent coefficients. The liquid-drop model calculation predicts $d_1 = 2/7b_1^2$ [34]. Previous STAR measurements suggest that $d_1 \beta_2^4$ is larger than $|c_1|$ in the 0%–5% most central collisions [44].

For higher-order flow harmonics ($n=3,4$), large statistical uncertainties in $c_3\{4\}$ and $c_4\{4\}$ preclude measuring ρ_3^{pcc} and ρ_4^{pcc} . Thus, the simpler normalization of equation (6) is used. For $n=2$ in central collisions and generally for $n=3$ and 4, $|c_n\{4\}| \ll c_n\{2\}^2$, so $\sqrt{\text{var}(v_n^2)} \approx \langle v_n^2 \rangle$ and $\rho_n^{\text{pcc}} \approx \rho_n$. However, in non-central collisions, $\sqrt{\text{var}(v_2^2)} < \langle v_2^2 \rangle$, leading to $\rho_2^{\text{pcc}} > \rho_2$. In peripheral collisions, their differences are more affected by non-flow.

Previous studies [16, 34] found that ρ_2 is nearly centrality-independent for spherical nuclei, making it ideal for detecting quadrupole deformation. This normalization also benefits from the simple dependence of $\langle v_2^2 \rangle$ on β_2 (equation (2)). In contrast, $\text{var}(v_2^2)$ has a more complex form:

$$\text{var}(v_2^2) = (a_1 + b_1 \beta_2^2)^2 - c_1 - d_1 \beta_2^4 \quad (10)$$

where a_1 and b_1 are from equation (2), and c_1 and d_1 are from equation (9). This complicates the interpretation of ρ_2^{pcc} in terms of quadrupole deformation.

All observables are computed for four p_T ranges: 0.2–2 GeV c^{-1} , 0.2–3 GeV c^{-1} , 0.5–2 GeV c^{-1} , and 0.5–3 GeV c^{-1} . Studying p_T range dependence helps illuminate non-flow effects, which are generally larger at higher p_T . Furthermore, the hydrodynamic response may vary with p_T -range due to sub-leading modes of the energy density fluctuations [11, 62]. These sub-leading modes could be sensitive

to the shape and radial structure of the colliding nuclei. These high-order geometric effects should be included (at least partially) by event-by-event hydrodynamic model simulations. Thus, observables measured in different p_T ranges are expected to provide consistent constraints on nuclear deformation.

2.3. Influence of non-flow correlations

Non-flow refers to correlations among a few particles from a common source (e.g. resonance decays, jets) that are uncorrelated with the initial geometry. Most non-flow sources are short-range (near-side), but dijet fragmentation can cause wider η correlations (away-side). The non-flow contribution generally increases with p_T , decreases for higher-order cumulants, and decreases with η gaps between particles. However, the η -gap dependence can also arise from longitudinal fluctuations.

Near-side non-flow is largely suppressed by the subevent method, which requires a large η gap. Remaining away-side non-flow can be estimated assuming independent sources, where non-flow in n -particle cumulants (\mathcal{O}) scales with charged particle multiplicity as $1/N_{\text{ch}}^{n-1}$:

$$\langle \mathcal{O} \rangle_{\text{nf}} \approx \frac{[\langle \mathcal{O} \rangle N_{\text{ch}}^{n-1}]_{\text{peri}}}{N_{\text{ch}}^{n-1}}, \quad (11)$$

where ‘peri’ denotes the N_{ch} range corresponding to the 90%–100% centrality bin. While widely used in small collision systems at RHIC and the LHC [63–67], this method may not be appropriate for large systems where jet quenching strongly modifies away-side correlations.

Following [16], non-flow is estimated by: (1) the difference between the standard method and subevent methods, and (2) the N_{ch} -scaling method (equation (11)). The latter is applied for $\langle v_n^2 \rangle$ and $\langle v_n^2 \delta p_T \rangle$, where medium effects redistribute non-flow azimuthally rather than suppress them. This approach is not suitable for $\langle (\delta p_T)^2 \rangle$, where medium effects should always suppress non-flow.

The subevent requirement reduces the values of $\langle v_n^2 \rangle$, $\langle (\delta p_T)^2 \rangle$, and $\langle v_n^2 \delta p_T \rangle$ in the most peripheral bin. Differences between standard and subevent methods are used to estimate residual non-flow in the subevent method. These differences, propagated to ratios between U+U and Au+Au, are 1.1%, 3.5%, and 11% for $R_{v_2^2}$, $R_{(\delta p_T)^2}$, and $R_{v_2^2 \delta p_T}$, respectively.

For non-flow estimation based on the N_{ch} -scaling method, we assume the entire signals in the 80%–100% centrality two-subevent results are non-flow, then estimate the non-flow fraction using equation (11). This is used for $\langle v_2^2 \rangle$ and $\langle v_2^2 \delta p_T \rangle$. In 0%–5% most central collisions, estimated non-flow is about 6% for $\langle v_2^2 \rangle$ and about 1.4% for $\langle v_2^2 \delta p_T \rangle$. Propagated to ratios, these are 2.8% for $R_{v_2^2}$ and 2.5% for $R_{v_2^2 \delta p_T}$.

Non-flow systematic uncertainties are taken as the larger of the two estimates for $R_{v_2^2}$ and $R_{v_2^2 \delta p_T}$, while for $R_{(\delta p_T)^2}$, the difference between standard and subevent methods is used. Total non-flow uncertainties in the 0%–5% centrality are 2.8%, 3.5% and 11% for $R_{v_2^2}$, $R_{(\delta p_T)^2}$ and $R_{v_2^2 \delta p_T}$, respectively.

Non-flow correlations are physical processes, not instrumental effects. Most flow measurements in large collision systems at RHIC and the LHC do not perform model-dependent non-flow subtractions. Ideally, non-flow physics should be incorporated into theoretical models used for comparison. Unfortunately, most models are unable to correctly describe the non-flow correlations (e.g. including contributions from resonance decays but not jet quenching). This should be taken into account when comparing measurements to models.

In this paper, non-flow systematics are treated as model-dependent uncertainties and are incorporated for quantitative extraction of nuclear shape parameters in section 4.2, but are otherwise not included in data plots.

2.4. Systematic uncertainties

Systematic uncertainties were estimated by varying track quality selections and collision z_{vtx} range, studying the influence of pileup, comparing results from different data-taking periods, and performing a closure test. The following summarizes uncertainties for the default p_T range (0.2–3 GeV c $^{-1}$).

Track selection: varying the number of fit hits on the track (16–19) and the DCA cut (< 3 cm to < 2.5 cm) yielded variations of 0.5%–1% for $\langle p_T \rangle$ and 1%–5% for $\langle (\delta p_T)^2 \rangle$. Uncertainties for $\langle v_n^2 \rangle$ reached 3%, 5%, and 10% for $n = 2, 3$, and 4, respectively, with larger relative uncertainties in central collisions due to smaller $\langle v_n^2 \rangle$ values. Track selection influences on $\langle v_n^2 \delta p_T \rangle$ lead to uncertainties up to 4% ($n = 2$), 10% ($n = 3$), and 20% ($n = 4$).

Collision vertex: comparing results for $|z_{\text{vtx}}| < 12$ cm with $|z_{\text{vtx}}| < 30$ cm showed differences of 0.2%–0.9% for $\langle p_T \rangle$ and 0.5%–3% for other observables.

Data-taking periods: comparisons between normal and reverse magnetic field runs in Au+Au collisions showed consistency within statistical uncertainties. Comparisons between the 2010 and 2011 Au+Au datasets, which have different active acceptances in the TPC, were largely consistent, within the quoted uncertainties, as a function of centrality. However, significant differences are observed in several cases. We observe about 0.1%, 1%–2%, 2%–4%, 2%, 2%–8% variations in $\langle p_T \rangle$, $\langle (\delta p_T)^2 \rangle$, $\langle v_2^2 \rangle$, $\langle v_3^2 \rangle$, and $\langle v_4^2 \rangle$, respectively. In addition, a 10%–15% variation of $\langle v_n^2 \delta p_T \rangle$ is also observed in central collisions. Half of the observed differences are included in the systematic uncertainties for each observable.

Pileup and background: varying the cut on the correlation between $N_{\text{ch}}^{\text{rec}}$ and TOF hits showed an influence of 1%–3% for $\langle v_n^2 \rangle$ and $\langle (\delta p_T)^2 \rangle$, and up to 2%–10% for $\langle v_n^2 \delta p_T \rangle$ in mid-central collisions.

Acceptance correction: as a cross-check, a re-centering correction on flow vectors [68] was applied instead of the ϕ -dependent acceptance correction, $\text{acc}_\eta(\phi)$. Results were consistent.

Closure test: a closure test was performed. Reconstruction efficiency and its variations in η and ϕ from data were used to retain a fraction of particles generated by a multi-phase transport model [69]. Observables were calculated with track-by-track weights (equation (7)) and compared to original particles. The observables $\langle v_n^2 \rangle$, $\langle p_T \rangle$, and $\langle (\delta p_T)^2 \rangle$ were recovered within statistical uncertainties. However, a 2%–4% non-closure was observed in $\langle v_2^2 \delta p_T \rangle$ and $\langle v_3^2 \delta p_T \rangle$, and up to 15% in $\langle v_4^2 \delta p_T \rangle$, which are included in the final systematic uncertainties.

Additional cross-checks: the track reconstruction efficiency has an approximate 5% uncertainty. Varying this efficiency resulted in variations of about 0.1% for $\langle p_T \rangle$. Variations for other observables were either less than 1% or within statistical uncertainties. The reconstructed p_T can differ from the true value due to finite momentum resolution. This was investigated by smearing the reconstructed p_T , calculating the observable, and comparing the results with the original ones. A discrepancy of approximately 0.1% and 0.5% was observed for $\langle p_T \rangle$ and $\langle (\delta p_T)^2 \rangle$, respectively. Other observables remained consistent within their statistical uncertainties.

Systematic uncertainties for other p_T ranges are similar, generally smaller for higher p_T ranges due to better track reconstruction efficiency and fewer fake tracks. However, a slightly larger difference between standard and subevent methods is observed at higher p_T due to larger non-flow.

These different sources are assumed to be independent, and are hence combined in quadrature to give the total systematic uncertainties. For measurements performed in $0.2 < p_T < 2$ or $0.2 < p_T < 3 \text{ GeV c}^{-1}$, total uncertainties for $\langle v_2^2 \rangle$, $\langle v_3^2 \rangle$, $\langle v_4^2 \rangle$, $\langle p_T \rangle$, $\langle (\delta p_T)^2 \rangle$, $\langle v_2^2 \delta p_T \rangle$, $\langle v_3^2 \delta p_T \rangle$, and $\langle v_4^2 \delta p_T \rangle$ are 1%–4%, 2%–8%, 4%–15%, 0.2%–1%, 1%–5%, 3%–8%, 5%–15% and 10%–20% respectively. Uncertainties are similar for 0.2 – 2 GeV c^{-1} and 0.3 – 2 GeV c^{-1} , but smaller for $0.5 < p_T < 2$ and $0.5 < p_T < 3 \text{ GeV c}^{-1}$.

Many uncertainty sources are similar in Au+Au and U+U collisions and partially cancel in the ratios between the two systems. However, detector stability, as assessed by comparing 2010 and 2011 Au+Au data, is incorporated without cancellation into the ratio calculation. Ratios are calculated for each source of systematic uncertainty, and variations are combined to give the total uncertainty on this ratio.

This paper presents results for $\langle v_n^2 \rangle$, $\langle v_n^2 \delta p_T \rangle$, $\langle p_T \rangle$, $\langle (\delta p_T)^2 \rangle$, and ρ_n , and their derived ratios between U+U and Au+Au. Results are presented by default as a function of centrality, with corresponding results as a function of N_{ch} included in the appendix. Statistical uncertainties are indicated by error bars, and systematic uncertainties by shaded boxes in all figures.

3. Results

3.1. General trends and the signatures of deformation

To isolate the effects of nuclear deformation, we compare results from collisions of highly-deformed ^{238}U with those of nearly-spherical ^{197}Au , as a function of centrality. The 20%

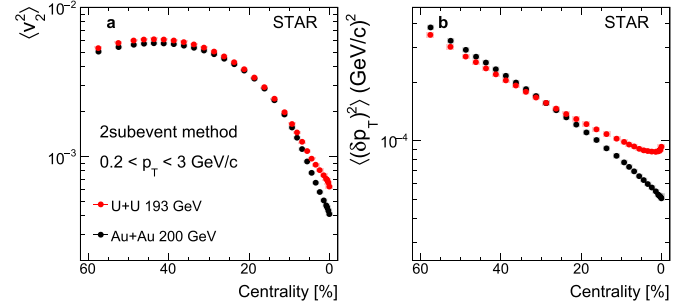


Figure 4. $\langle v_2^2 \rangle$ (left) and $\langle (\delta p_T)^2 \rangle$ (right) as a function of centrality in U+U and Au+Au collisions for charged hadrons in $0.2 < p_T < 3 \text{ GeV c}^{-1}$. Results are obtained using the two-subevent method.

difference in mass number between these nuclei is expected to have a minor influence on the hydrodynamic response [18], ensuring that observed differences at the same centrality are primarily sensitive to nuclear deformation.

Figure 4 shows a significant enhancement of $\langle v_2^2 \rangle$ and $\langle (\delta p_T)^2 \rangle$ in central U+U collisions compared to central Au+Au collisions. This enhancement is attributed to increased fluctuations in elliptic and radial flow driven by the large prolate deformation of ^{238}U (equation (2)). In contrast, figure 5 displays much smaller differences in $\langle v_3^2 \rangle$, $\langle v_4^2 \rangle$, and $\langle p_T \rangle$ between the two systems, which are expected since quadrupole deformation minimally impacts these observables.

However, $\langle v_3^2 \rangle$ values in central collisions are about 7% larger in U+U compared to Au+Au. This result is surprising. Naively, we expect the Au+Au system, being smaller, to have larger fluctuations in its initial geometry (specifically, larger $\langle \varepsilon_3^2 \rangle$). This simple scaling, $\langle \varepsilon_3^2 \rangle \propto 1/A$, suggests that $\langle v_3^2 \rangle_{\text{Au}}$ should be greater than $\langle v_3^2 \rangle_{\text{U}}$.

While greater viscous damping in the smaller Au+Au system would slightly reduce its v_3 compared to U+U, transport models still predict a slightly larger $\langle v_3^2 \rangle$ (by about 10%) for Au+Au, even after accounting for this effect [15]. On the other hand, this unexpected ordering of v_3 values can be explained by including a small amount of octupole deformation in the uranium nucleus; this octupole deformation would increase $v_{3\text{U}}$, as shown in equation (3). Hydrodynamic model calculations support this, confirming that a 7% larger $\langle v_3^2 \rangle$ in U+U is consistent with an octupole deformation parameter of $\beta_{3\text{U}} \sim 0.08$ – 0.10 [36].

Similar considerations apply to the ordering of $\langle v_4^2 \rangle$. Although the measurement uncertainties are larger for this observable, some impact from the hexadecapole deformation $\beta_{4\text{U}}$ might be expected. However, transport model calculations suggest that the expected larger fluctuation in Au+Au collisions is largely canceled by the stronger viscous damping [15]. This could result in $\langle v_4^2 \rangle$ being very similar in the two collision systems. Hence, the data suggest that the impact of $\beta_{4\text{U}}$ on $\langle v_4^2 \rangle$ is not significant compared to the measurement uncertainties.

The $\langle p_T \rangle$ values are slightly larger in U+U collisions, consistent with a denser QGP medium due to uranium's larger mass number. The sharp increase in $\langle p_T \rangle$ toward the most

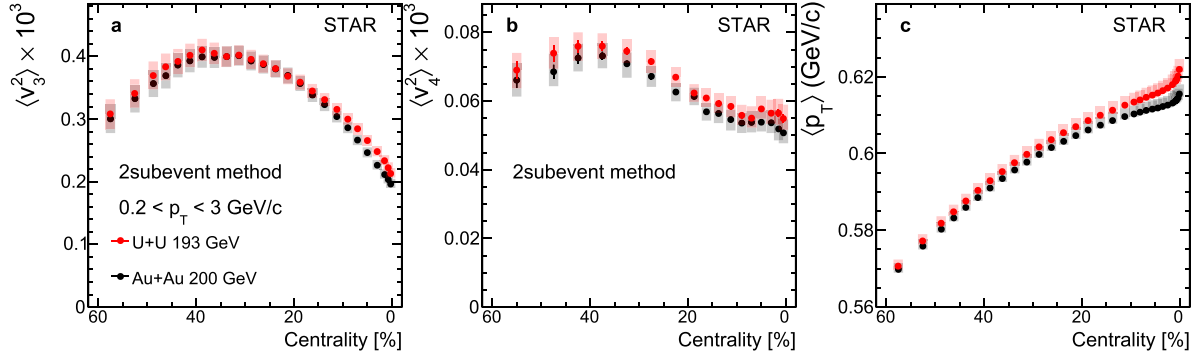


Figure 5. The $\langle v_3^2 \rangle$ (left), $\langle v_4^2 \rangle$ (middle) and $\langle p_T \rangle$ (right) as a function of centrality in U+U and Au+Au collisions for charged hadrons in $0.2 < p_T < 3 \text{ GeV c}^{-1}$.

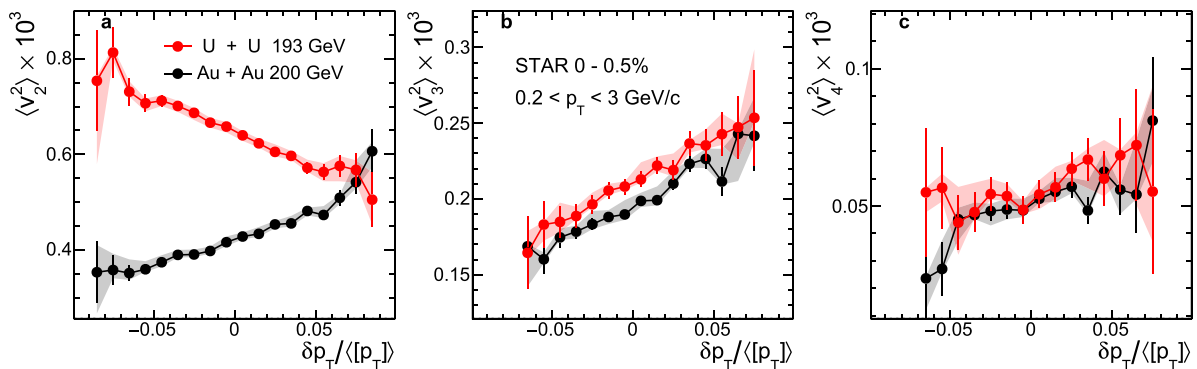


Figure 6. The $\langle v_2^2 \rangle$ (left), $\langle v_3^2 \rangle$ (middle) and $\langle v_4^2 \rangle$ (right) as a function of $\delta p_T / \langle [p_T] \rangle$ in the 0%–0.5% most central Au+Au (black) and U+U (red) collisions for charged hadrons in $0.2 < p_T < 3 \text{ GeV c}^{-1}$. Results are obtained using the two-subevent method.

central collisions may be linked to genuine temperature fluctuations [70]. These fluctuations, when convoluted with a steeply falling N_{ch} distribution, lead to an increase in $\langle p_T \rangle$ [71, 72]. It will be interesting to investigate whether this increase could also be influenced by nuclear deformation.

To visualize the expected shape-size correlation from figure 1, we examine the 0%–0.5% most central collisions, where nuclear deformation has the greatest impact. These events are binned according to their event-by-event δp_T values, and the corresponding $\langle v_n^2 \rangle$ values are shown in figure 6. The positive correlation between v_2 and δp_T in Au+Au collisions aligns with the positive correlation between ε_2 and d_\perp [34, 73]. Conversely, the decrease of v_2 with increasing δp_T in U+U collisions supports the picture in figure 1 [32]: events with small (large) $[p_T]$ are enriched with body–body (tip–tip) collisions. This is a dramatic effect: $\langle v_2^2 \rangle$ in U+U is over 60% higher than in Au+Au at the low end of δp_T , but nearly identical at the high end. The v_3 and v_4 values are similar in the two systems and largely unaffected by quadrupole deformation.

The linear correlation between v_n and δp_T with a slope of h in figure 6 can be directly related to ρ_n . We can express the linear relationship as $v_n^2 / \langle v_n^2 \rangle - 1 = h \delta p_T / \langle [p_T] \rangle$. Multiplying both sides by δp_T and averaging over the event ensemble,

we get $\langle v_n^2 \delta p_T \rangle / \langle v_n^2 \rangle = h \langle (\delta p_T)^2 \rangle / \langle [p_T] \rangle$. This leads to $\rho_n = h \sqrt{\langle (\delta p_T)^2 \rangle / \langle [p_T] \rangle}$, implying that ρ_n captures the linear correlation in figure 6.

The calculation of ρ_n and ρ_n^{pcc} requires $\langle v_n^2 \rangle$, $\sqrt{\text{var}(v_n^2)}$, $\sqrt{\langle (\delta p_T)^2 \rangle}$ and $\langle v_n^2 \delta p_T \rangle$; these components for $n=2$ are shown in figure 7 as a function of centrality. Central U+U collisions show significant enhancements in $\langle v_2^2 \rangle$, $\sqrt{\text{var}(v_2^2)}$, and $\sqrt{\langle (\delta p_T)^2 \rangle}$ relative to Au+Au, consistent with a large β_{2U} . Conversely, $\langle v_2^2 \delta p_T \rangle$ values are suppressed in U+U collisions across all centralities, consistent with a large β_{2U} and a prolate shape (equation (2)). In central collisions, where the Au+Au baseline is positive, the uranium’s deformation drives $\langle v_2^2 \delta p_T \rangle$ negative in the 0%–7% centrality range.

From these components, we calculate ρ_2 and ρ_2^{pcc} and present them in the bottom row of figure 7. The ρ_2 values in Au+Au collisions remain nearly constant across centrality, while in U+U they decrease gradually up to 15% centrality, then drop sharply in more central collisions. The ρ_2^{pcc} values in Au+Au collisions decrease slowly toward central collisions, largely unrelated to nuclear deformation. These behaviors are defining features of ρ_2 and ρ_2^{pcc} , and are robust against correlation methods and p_T selection (see section 3.2).

A similar study for higher-order harmonic flow is presented in figure 8, which shows $\langle v_n^2 \delta p_T \rangle$ and ρ_n for $n=3$ and 4 as

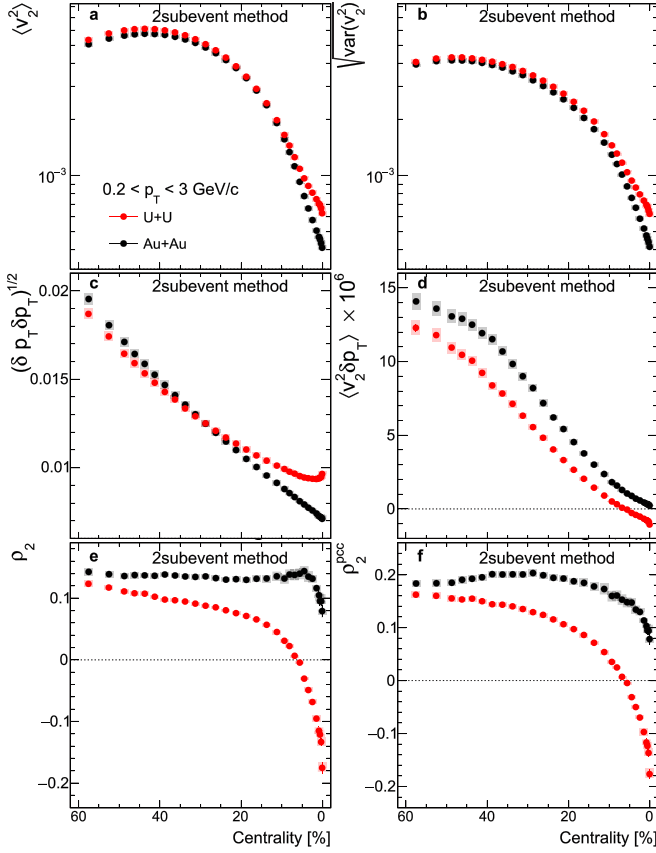


Figure 7. Centrality dependence of $\langle v_2^2 \rangle$, $\sqrt{\text{var}(v_2^2)}$, $\sqrt{\langle (\delta p_T)^2 \rangle}$, $\langle v_2^2 \delta p_T \rangle$ and derived quantities ρ_2 (equation (6)) and ρ_2^{pcc} (equation (5)) in Au+Au and U+U collisions. All are obtained using the two-subevent method. Note that the $\langle v_2^2 \rangle$ and $\sqrt{\langle (\delta p_T)^2 \rangle}$ data are taken directly from figure 4.

a function of centrality. While generally similar between systems, $\langle v_3^2 \delta p_T \rangle$ and ρ_3 values are smaller in central U+U collisions, qualitatively compatible with a small octupole deformation in ^{238}U via equation (3) [36].

3.2. Dependence on correlation methods and kinematic selections

All results so far utilize the two-subevent method. The impact of short-range non-flow correlations on $\langle v_n^2 \delta p_T \rangle$ is quantified by comparing the standard, two-subevent, and three-subevent methods. These comparisons are shown in figure 9 for ρ_2^{pcc} and ρ_2 , and in figure 10 for ρ_3 and ρ_4 . Note that $\langle v_n^2 \rangle$ and $\langle (\delta p_T)^2 \rangle$ in these comparisons are always calculated with the two-subevent method, so method variations in ρ_n originate solely from $\langle v_n^2 \delta p_T \rangle$.

In the 30%–60% centrality range, notable discrepancies between the standard and subevent methods reflect non-flow and longitudinal fluctuations. These differences are modest for $n = 2$ but larger for $n = 3$ and 4. Most variations occur between the standard and two-subevent methods, with generally smaller differences between the two- and three-subevent methods,

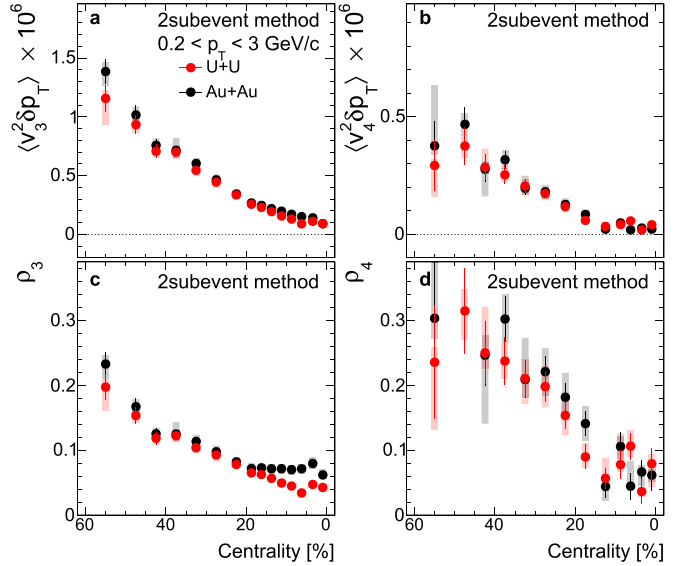


Figure 8. Centrality dependence of $\langle v_n^2 \delta p_T \rangle$ (top) and ρ_n (bottom) for $n = 3$ (left) and $n = 4$ (right) in Au+Au and U+U collisions. All are obtained using the two-subevent method.

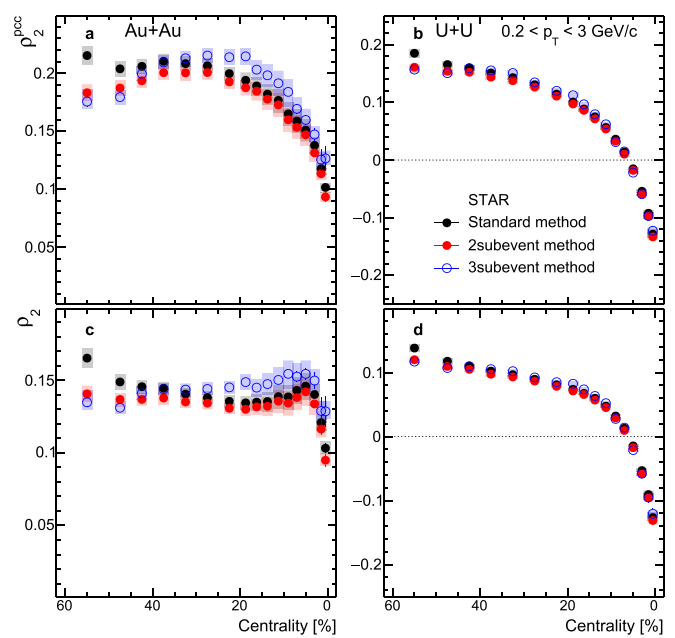


Figure 9. Centrality dependence of ρ_2^{pcc} (top) and ρ_2 (bottom) in Au+Au (left) and U+U (right) collisions, compared between the standard (black), two-subevent (red) and three-subevent methods (blue).

except in peripheral collisions where statistical precision is poor.

Figure 11 shows ρ_2^{pcc} and ρ_2 in four p_T intervals, revealing significant variations (around 20%) with the p_T selection. These variations reflect incomplete cancellation of final-state effects between the numerators and denominators, resulting from differences in the expected hydrodynamic responses. Key features include: (1) ρ_2^{pcc} and ρ_2 values increase when the

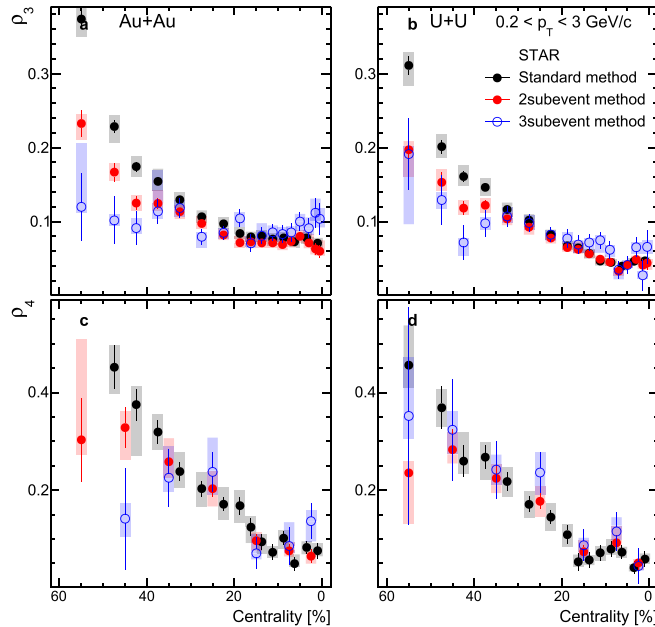


Figure 10. The normalized quantities ρ_3 (top) and ρ_4 (bottom) via equation (6) in Au+Au (left) and U+U (right) collisions, compared between the standard (black), two-subevent (red) and three-subevent methods (blue).

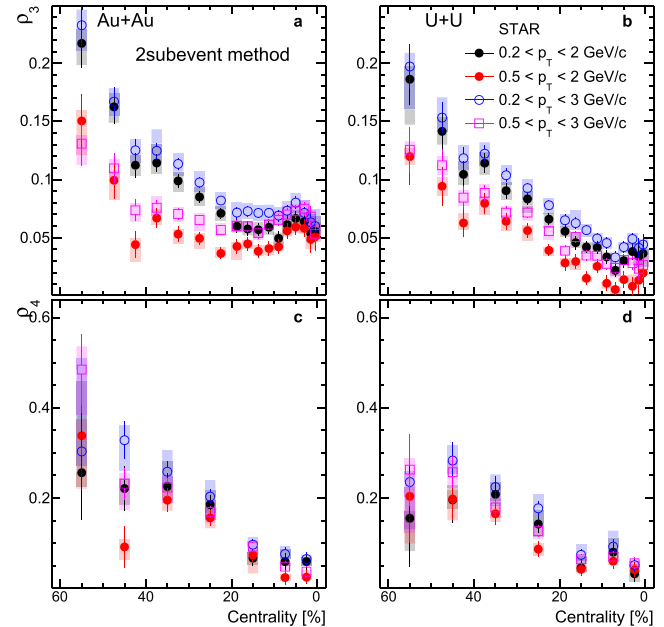


Figure 12. Centrality dependence of normalized quantities ρ_3 (top) and ρ_4 (bottom) via equation (6) in Au+Au (left) and U+U (right) collisions, calculated in four p_T intervals.

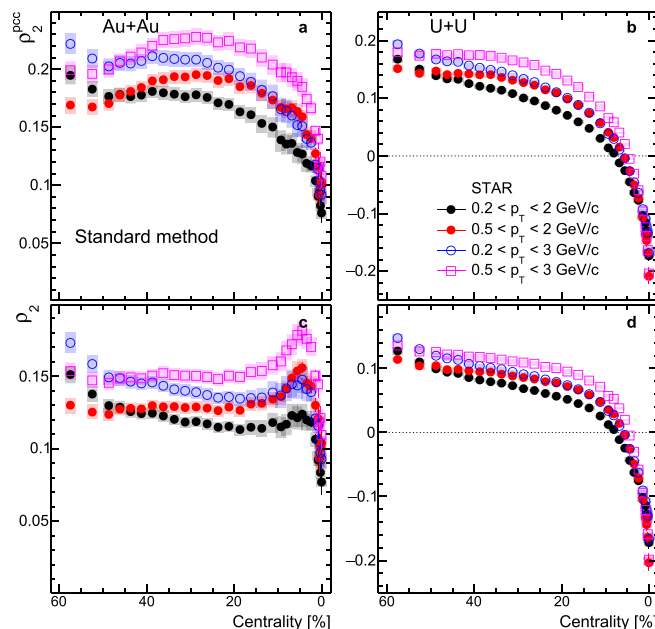


Figure 11. Centrality dependence of normalized quantities ρ_2^{pec} via equation (5) (top) and ρ_2 via equation (6) (bottom) in Au+Au (left) and U+U (right) collisions, calculated in four p_T intervals.

p_T interval's lower or upper end is raised, similar to observations in the Xe+Xe and Pb+Pb collisions at the LHC [60]. (2) Both observables decrease sharply in the UCC region in both systems. This sharp decrease, also observed at the LHC, can be attributed to centrality smearing due to the finite centrality resolution associated with N_{ch}^{rec} [35]. (3) ρ_2 exhibits a peak around 5% centrality in Au+Au, more pronounced when the

lower end of the p_T interval is raised. This increasing trend is potentially due to the moderately oblate deformation of Au nuclei [34].

A similar study for ρ_3 and ρ_4 is presented in figure 12, based on the two-subevent method. The values of ρ_3 increase when raising the higher end of the p_T interval, but decrease when raising the lower end, opposite to the behavior observed for ρ_2 . In the UCC region, ρ_3 values in Au+Au collisions are systematically larger than in U+U collisions. The p_T dependence of ρ_4 is similar to that for ρ_3 , but statistical uncertainties are too large for quantitative evaluation.

3.3. Ratios between the two systems

While normalized observables like ρ_n reduce final-state effects, they do not fully cancel them, as indicated by their sensitivities to the p_T selection. A more robust approach involves direct ratios of the same observable between U+U and Au+Au (equation (4)) at matching centrality. These ratios also reduce the influence of initial-state properties common to both U and Au, such as nucleon sizes, nucleon distances, and nucleon substructure fluctuations.

Figure 13 presents ratios of one- and two-particle observables. Although individual observables, such as $\langle v_n^2 \rangle$ and $\langle (\delta p_T)^2 \rangle$, can change by over a factor of two across the four p_T intervals, their ratios are remarkably p_T -independent, suggesting significant cancellation of final-state effects. In central collisions, $R_{v_2^2}$ and $R_{(\delta p_T)^2}$ show a dramatic increase due to uranium's larger deformation (equation (2)). The centrality range for this increase is narrow for $R_{v_2^2}$ (0%–10%) but much wider for $R_{(\delta p_T)^2}$ (0%–30%). This difference arises because $\langle v_2^2 \rangle$ in non-central collisions is dominated by the

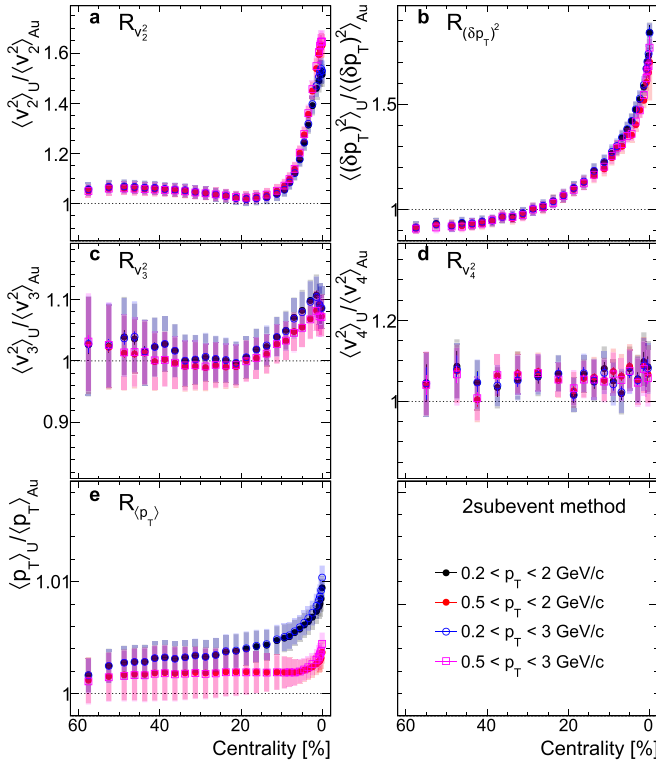


Figure 13. Centrality dependence of ratios of $\langle v_2^2 \rangle$, $\langle (\delta p_T)^2 \rangle$, $\langle v_3^2 \rangle$, $\langle v_4^2 \rangle$ and $\langle p_T \rangle$ between U+U and Au+Au collisions in four p_T ranges.

elliptic shape of the overlap region, thereby diluting the impact of nuclear deformation. In contrast, $\langle (\delta p_T)^2 \rangle$ is not affected by this average geometry [74]. The ratio $R_{v_3^2}$ shows a slight increase in central collisions, possibly from octupole deformation in Uranium, while $R_{v_4^2}$ shows no centrality-dependent modification.

The $\langle p_T \rangle$ ratio increases slightly (about 1%) toward central collisions, possibly due to a denser medium in U+U collisions and a bias towards tip-tip collisions in UCC [44]. Note that p_T interval choice affects $\langle p_T \rangle$, with increasing lower p_T limits naturally lowering $\langle p_T \rangle$. This kinematic effect dilutes the increase in the UCC region, accounting for the split of the ratios into two groups based on the lower p_T limit. Changing the upper limit has minimal impact due to the relatively fewer particles at high p_T .

Figure 14 shows the ratio of $\langle v_n^2 \delta p_T \rangle$ between U+U and Au+Au for standard and subevent methods. Figure 15 shows the same ratio for four p_T intervals. In mid-central and peripheral collisions, $R_{v_n^2 \delta p_T}$ values are independent of the method and p_T interval, but modest dependencies appear in the UCC region.

Many ratios in figures 13–15 deviate significantly from unity in the UCC region. As mentioned earlier and discussed in section 4, these deviations can be used to constrain the quadrupole and higher-order deformation of ^{238}U .

A challenge in this analysis is that observables are dominated by baseline contributions from spherical nuclei (a_n terms

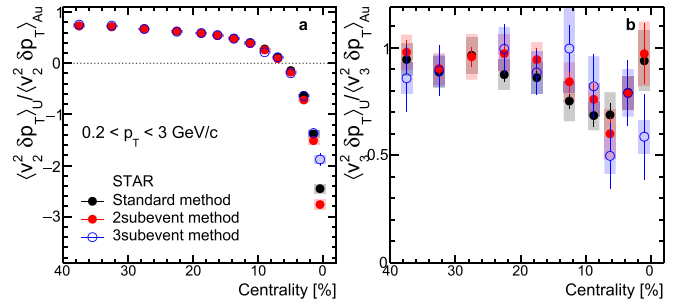


Figure 14. Centrality dependence of ratios of $\langle v_2^2 \delta p_T \rangle$ (left) and $\langle v_3^2 \delta p_T \rangle$ (right) between U+U and Au+Au collisions, compared between different methods in $0.2 < p_T < 3 \text{ GeV c}^{-1}$.

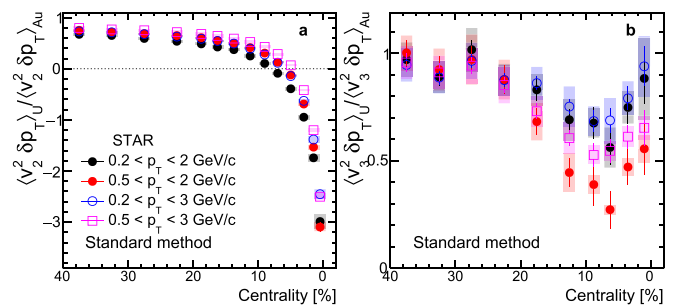


Figure 15. Centrality dependence of ratios of $\langle v_2^2 \delta p_T \rangle$ (left) and $\langle v_3^2 \delta p_T \rangle$ (right) between U+U and Au+Au collisions, obtained for four p_T intervals.

in equations (2)), which are strong functions of impact parameter and increase rapidly towards more peripheral collisions. In contrast, deformation-related terms (b_n terms) are largest in central collision and decrease slowly towards peripheral collisions [15, 34]. Therefore, the ratios and their centrality dependencies discussed above largely reflect impact parameter dependencies.

To remove the a_n terms, which have similar values in U+U and Au+Au, we calculate baseline-subtracted ratios [34]:

$$\rho_2^{\text{sub}} = \frac{\langle v_2^2 \delta p_T \rangle_U - \langle v_2^2 \delta p_T \rangle_{\text{Au}}}{(\langle v_2^2 \rangle_U - \langle v_2^2 \rangle_{\text{Au}}) \sqrt{\langle (\delta p_T)^2 \rangle_U - \langle (\delta p_T)^2 \rangle_{\text{Au}}}},$$

$$\rho_2^{\text{pcc,sub}} = \frac{\langle v_2^2 \delta p_T \rangle_U - \langle v_2^2 \delta p_T \rangle_{\text{Au}}}{\sqrt{\text{var}(v_2^2)_U - \text{var}(v_2^2)_{\text{Au}}} \sqrt{\langle (\delta p_T)^2 \rangle_U - \langle (\delta p_T)^2 \rangle_{\text{Au}}}}}. \quad (12)$$

This difference $\Delta \mathcal{O} = \mathcal{O}_U - \mathcal{O}_{\text{Au}}$ cancels most spherical baseline contributions while isolating the deformation component:

$$\rho_2^{\text{sub}} \approx -\frac{b_3 (\cos(3\gamma_U) \beta_{2U}^3 - \cos(3\gamma_{\text{Au}}) \beta_{2\text{Au}}^3)}{b_1 \sqrt{b_2} (\beta_{2U}^2 - \beta_{2\text{Au}}^2)^{3/2}} \\ \xrightarrow{\beta_{2\text{Au}} \rightarrow 0} -\frac{b_3}{b_1 \sqrt{b_2}} \cos(3\gamma_U). \quad (13)$$

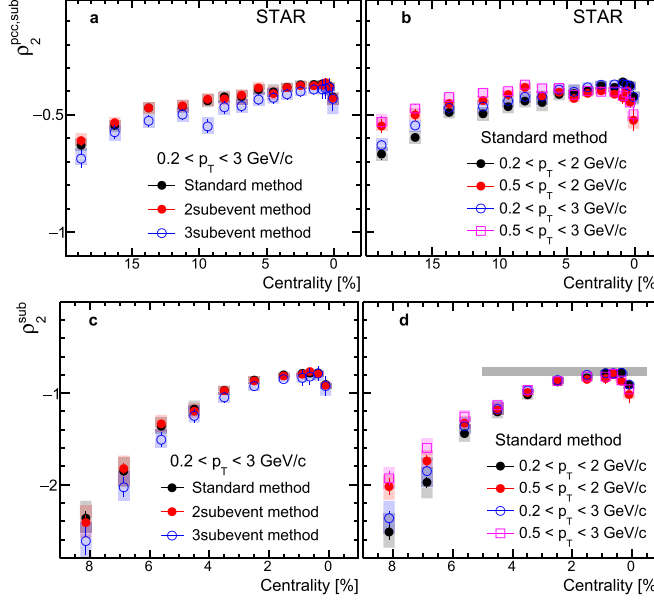


Figure 16. Centrality dependence of the baseline-subtracted and normalized quantities $\rho_2^{\text{pcc,sub}}$ (top) and ρ_2^{sub} (bottom) defined via equation (12). They are compared between different methods in $0.2 < p_T < 3 \text{ GeV } c^{-1}$ (left) or four p_T intervals (right). The thick gray line in the bottom right panel indicates the expectation from the liquid drop model estimation at -0.76 (see text).

A liquid-drop model estimates the coefficients $-\frac{b_3}{b_1\sqrt{b_2}} = -\sqrt{10}/7$ [34]. In this limit, $\rho_2^{\text{sub}} = -0.76$ assuming $(\beta_{2\text{U}}, \gamma_{\text{U}}) = (0.28, 0^\circ)$ and $(\beta_{2\text{Au}}, \gamma_{\text{Au}}) = (0.14, 45^\circ)$. The second line of equation (13) shows that in the large $\beta_{2\text{U}}$ limit and ignoring $\beta_{2\text{Au}}$, ρ_2^{sub} depends only on uranium's triaxiality.

The subtraction method is valid when the baseline difference is much smaller than the deformation contribution. This holds for $\langle v_2^2 \delta p_T \rangle$ over a wide centrality range, but only a limited range for $\langle v_2^2 \rangle$ (0%–5%), $\sqrt{\text{var}(v_2^2)}$ (0%–10%), and $\langle (\delta p_T)^2 \rangle$ (0%–20%), see figure 7.

The interpretation of $\rho_2^{\text{pcc,sub}}$ is more complex due to a more involved form for $\text{var}(v_2^2)$ derived from equation (10). Assuming identical a_1 , b_1 , c_1 and $d_1 = 2/7b_1^2$ for the two collision systems:

$$\Delta \text{var}(v_2^2) = b_1^2 (\beta_{2\text{U}}^2 - \beta_{2\text{Au}}^2) (2a_1/b_1 + 5/7(\beta_{2\text{U}}^2 + \beta_{2\text{Au}}^2)) \dots \quad (14)$$

we obtain:

$$\begin{aligned} \rho_2^{\text{pcc,sub}} &\approx -\frac{b_3 (\cos(3\gamma_{\text{U}})\beta_{2\text{U}}^3 - \cos(3\gamma_{\text{Au}})\beta_{2\text{Au}}^3)}{b_1 \sqrt{b_2 (2a_1/b_1 + 5/7(\beta_{2\text{U}}^2 + \beta_{2\text{Au}}^2))} (\beta_{2\text{U}}^2 - \beta_{2\text{Au}}^2)} \\ &\xrightarrow{\beta_{2\text{Au}} \rightarrow 0} -\frac{b_3 \beta_{2\text{U}}}{b_1 \sqrt{b_2 (2a_1/b_1 + 5/7\beta_{2\text{U}}^2)}} \cos(3\gamma_{\text{U}}) . \end{aligned} \quad (15)$$

The a_1/b_1 term, affected by the spherical baseline, reduces the magnitude of $\rho_2^{\text{pcc,sub}}$ relative to ρ_2^{sub} . Also, $\rho_2^{\text{pcc,sub}}$ can be obtained over a wider centrality range because the centrality interval over which $\Delta \text{var}(v_2^2) > 0$ is wider than that for $\Delta \langle v_2^2 \rangle > 0$ (see figure 7).

Figure 16 shows $\rho_2^{\text{pcc,sub}}$ and ρ_2^{sub} in central collisions. These observables are robust against variations in correlation methods and p_T intervals. They are negative over a significantly wider centrality range than the original observables ρ_2^{pcc} and ρ_2 . Furthermore, the values of ρ_2^{sub} in the UCC region are remarkably close to the analytical liquid-drop limit of -0.76.

4. Model comparisons

4.1. Comparisons with initial-state and hydrodynamic models for v_n – p_T correlations

The correlation between v_n and $[p_T]$ arises from hydrodynamic responses to correlated fluctuations between elliptic eccentricity, ε_2 , and the inverse of the transverse area, d_\perp . Most flow observables are influenced by both initial-state geometry and final-state QGP evolution.

Initial state model. Models that consider only the initial state, such as the Glauber model, rely on linear response relations: $v_n \propto \varepsilon_n$ and $\delta p_T/p_T \propto \delta d_\perp/d_\perp$. These relations yield estimators for ρ_2 and ρ_2^{pcc} in terms of eccentricity and d_\perp [11, 75]:

$$\begin{aligned} \hat{\rho}_2 &= \frac{\langle \varepsilon_2^2 \delta d_\perp/d_\perp \rangle}{\langle \varepsilon_2^2 \rangle \sqrt{\langle (\delta d_\perp/d_\perp)^2 \rangle}} \\ \hat{\rho}_2^{\text{pcc}} &= \frac{\langle \varepsilon_2^2 \delta d_\perp/d_\perp \rangle}{\sqrt{\text{var}(\varepsilon_2^2)} \sqrt{\langle (\delta d_\perp/d_\perp)^2 \rangle}} . \end{aligned} \quad (16)$$

Similarly, ratios between U+U and Au+Au, mimicking $R_{v_2^2 \delta p_T}$ or R_{ρ_2} (equation (4)), as well as the subtracted forms

Table 1. Choices of Woods–Saxon parameters, including nuclear deformations, in the Glauber and IP-Glasma+MUSIC models. Default values are in bold; the rest are variations to constrain (β_{2U}, γ_U) and their theoretical uncertainties, especially for the IP-Glasma+MUSIC model discussed in section 4.2.

model	species	R_0 (fm)	a (fm)	β_2	β_4	γ (°)
Glauber	^{197}Au	6.62	0.52	0.14	0	30, 45 , 60
	^{238}U	6.81	0.55	0, 0.15, 0.22	0	0 , 10, 15
				0.28 , 0.34	0.09	20, 25
Hydro	^{197}Au	6.62 , 6.38	0.52	0.14 , 0.12	0	37, 45 , 53
	^{238}U	6.81 , 7.07	0.55	0, 0.15	0	0 , 10
				0.22, 0.25	0.09	15, 20
				0.28 , 0.34		

to mimic ρ_2^{sub} and $\rho_2^{\text{pcc,sub}}$, can be formed.

$$\begin{aligned} \hat{\rho}_2^{\text{sub}} &= \frac{\Delta \langle \varepsilon_2^2 \delta d_\perp / d_\perp \rangle}{\Delta \langle \varepsilon_2^2 \rangle \sqrt{\Delta \langle (\delta d_\perp / d_\perp)^2 \rangle}} \\ \hat{\rho}_2^{\text{pcc,sub}} &= \frac{\Delta \langle \varepsilon_2^2 \delta d_\perp / d_\perp \rangle}{\sqrt{\Delta \text{var}(\varepsilon_2^2)} \sqrt{\Delta \langle (\delta d_\perp / d_\perp)^2 \rangle}}. \end{aligned} \quad (17)$$

Here, $\Delta \mathcal{O}$ represents the difference of an observable \mathcal{O} between U+U and Au+Au collisions. For this study, we use the standard quark Glauber model [76] with deformation parameters from [34]. These normalized quantities serve as estimators for the corresponding ratios of final-state observables and do not capture final-state effects in the data (figure 11).

Full hydrodynamic simulations. Final-state effects can be quantified using full event-by-event hydrodynamic model simulations with realistic initial conditions. We utilize the state-of-the-art IP-Glasma+MUSIC model [11, 77], which dynamically generates initial conditions from the gluon saturation model (IP-Glasma) and simulates full 3D viscous hydrodynamics via the MUSIC code. Final-state particles are generated using the Cooper-Frye prescription for hadronization, followed by UrQMD hadronic transport. This model is computationally expensive, so it can only be studied with limited statistics.

Nuclear structure setup. Table 1 details the Woods–Saxon parameters, including nuclear deformation for Au and U, used in the Glauber and IP-Glasma+MUSIC models. Nucleon-nucleon inelastic cross-sections are 40.6 mb for U+U at 193 GeV and 42 mb for Au+Au at 200 GeV. Following [16, 30], we set default ^{197}Au parameters as $\beta_{2\text{Au}} = 0.14$ and $\gamma_{\text{Au}} = 45^\circ$. For ^{238}U , known for its prolate deformation and moderate hexadecapole deformation from low-energy experiments and calculations, we can β_{2U} values from 0 to 0.34 in both models. We also vary β_{4U} (0–0.09), γ_U (0° – 30°), and γ_{Au} (30° – 60°) to test sensitivity to hexadecapole deformation and triaxiality. Variations of other structure parameters are only used in section 4.2 for quantitative estimation of

deformation parameters. Approximately 50 million Glauber events are generated following [34] and 100 000–400 000 IP-Glasma+MUSIC events are generated for each parameter set, using the code provided by the authors of [11, 77]. About 5% of these generated events end up in the UCC region. Each IP-Glasma+MUSIC event is oversampled at least 100 times to minimize non-flow and statistical fluctuations in the hadronic transport.

Comparison of ρ_2^{pcc} and ρ_2 . Figure 17(a) compares ρ_2^{pcc} in the $0.2 < p_T < 3 \text{ GeV c}^{-1}$ range with IP-Glasma+MUSIC for varying β_{2U} . While the model over-predicts data in peripheral collisions, prolate deformation significantly reduces ρ_2 in more central collisions. For $\beta_{2U} = 0.28$, the model predicts a zero-crossing around 7% centrality, consistent with data. This zero-crossing point serves as an important anchor, as it is (by construction) independent of normalization and correlation methods, and weakly dependent on p_T selections (figure 11).

Figure 17(b) shows the comparison with Glauber model estimators $\hat{\rho}_2^{\text{pcc}}$. The magnitude and trend of the Glauber model are similar to the IP-Glasma+MUSIC model, indicating a dominance of initial conditions on the behavior of ρ_2^{pcc} . The Glauber model also correctly predicts the zero-crossing location. Both models predict a steeper decrease in the UCC region than observed in the data, likely due to weaker centrality smearing in the models. Hexadecapole deformation mildly reduces $\hat{\rho}_2^{\text{pcc}}$ in non-central collisions.

Figure 17(c) investigates the impact of triaxiality. Data are compared to Glauber calculations for $\beta_{2U} = 0.28$ and $\beta_{2\text{Au}} = 0.14$ with varying triaxiality. Increasing γ raises ρ_2^{pcc} in the 0%–20% centrality range in U+U, shifting the zero-crossing point towards more central collisions. Au+Au results are less sensitive to γ due to the smaller $\beta_{2\text{Au}}$.

Figure 18 presents the same comparison for ρ_2 . The IP-Glasma+MUSIC model predicts a flat centrality dependence for Au+Au, consistent with data, though with a larger magnitude. For small β_2 values, both models (especially Glauber) predict a slight peak around 3% centrality, more pronounced than in the data.

We attribute the modest discrepancies between models and data for ρ_2^{pcc} and ρ_2 to residual final-state effects, not included in the Glauber model [11, 77] and not fully captured by the IP-Glasma+MUSIC model [11]. Example of such effects could

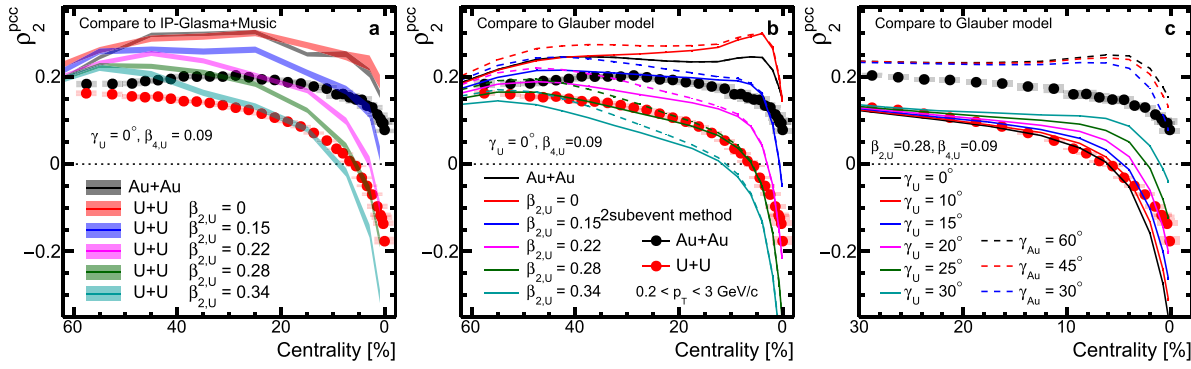


Figure 17. ρ_2^{pcc} in Au+Au (black symbols) and U+U (red symbols) collisions from $0.2 < p_T < 3 \text{ GeV c}^{-1}$ range, compared with IP-Glasma+MUSIC hydrodynamic model (left) and Glauber model calculation (middle) with $\gamma_U = 0^\circ$ and different β_{2U} values, and Glauber model calculation with $\beta_{2U} = 0.28$ and different γ_U and γ_{Au} (right). In all cases, $\beta_{2\text{Au}}$ is fixed at 0.14, and $\beta_{4\text{U}} = 0.09$, except in the middle panel where $\beta_{4\text{U}} = 0$ (dashed lines) are also shown.

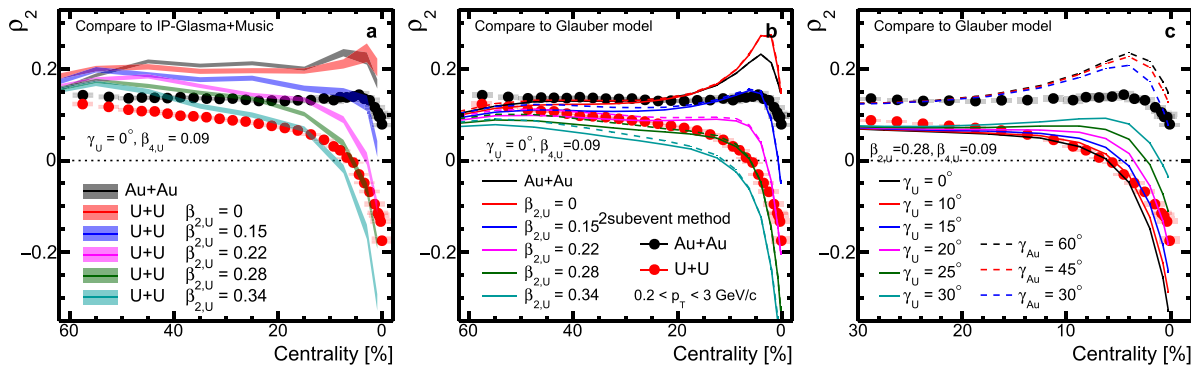


Figure 18. Same as figure 17 but for ρ_2 .

be subleading flow [62] or non-linear effects between ε_n and v_n and between δd_\perp and $\delta[p_T]$ [78].

Ratios Between U+U and Au+Au. Incomplete cancellation of final-state effects is expected as hydrodynamic responses are observable-dependent and thus differ between numerators and denominators. Ratios of the same quantity between U+U and Au+Au are expected to cancel most residual sensitivities and model dependencies in initial conditions, making them more sensitive to genuine nuclear structure effects.

Figure 19 compares ratios for ρ_2 and $\langle v_2^2 \delta p_T \rangle$ with model calculations. IP-Glasma+MUSIC with $\beta_{2U} = 0.28$ (top row) agrees with data over a much wider centrality range than that in figures 17 and 18. The Glauber model (middle row) also shows much better agreement. Centrality smearing effects in the UCC region are expected to be similar between Au+Au and U+U collisions [35], reducing their impact in ratios and leading to better model agreement compared to figures 17 and 18. The bottom row demonstrates the sensitivity of these ratios to γ_U in the Glauber model. A triaxiality of more than 15° would visibly shift the zero-crossing point and cause strong deviations from data, also supporting a prolate shape for the ^{238}U nucleus.

We have observed that R_{ρ_2} and $R_{v_2^2 \delta p_T}$ have small residual dependencies on the choice of p_T intervals. These p_T dependencies, especially the relative ordering between different p_T

intervals, are well-reproduced by the IP-Glasma+MUSIC (figure 20). This further validates the use of these ratios for constraining uranium deformation.

Figure 21 show IP-Glasma+MUSIC predictions for ρ_3 and ρ_4 . The model provides a qualitative description of the trends in the data.

Comparison for observables obtained via the subtraction method. section 3.3 introduced subtracted observables (ρ_2^{sub} , $\rho_2^{\text{pcc,sub}}$) to remove spherical baseline contributions and expose the impact of triaxiality. Figures 22 and 23 compare these subtracted quantities with IP-Glasma+MUSIC, and figure 24 shows the comparison with Glauber model.

For sufficiently large β_{2U} ($\gtrsim 0.28$), $\rho_2^{\text{pcc,sub}}$ and ρ_2^{sub} in the UCC region should approach a limiting value dependent only on γ_U (equations (13) and (15)). IP-Glasma+MUSIC predictions for $\beta_{2U} = 0.28$ and 0.34 indeed converge in the 0%–5% centrality range (figure 22). Deviations in less central collisions are expected due to incomplete subtraction of spherical baseline, unrelated to deformation. Increasing γ_U also increase these observables (figure 23); a relatively small triaxiality ($\gamma_U \lesssim 15^\circ$) is preferred by the data.

This limiting behavior can be studied with better statistical precision in the Glauber model (figure 24). The top panels compare data with calculation for different β_{2U} and β_{4U} with fixed $\gamma_U = 0^\circ$. Glauber predictions for $\beta_{2U} =$

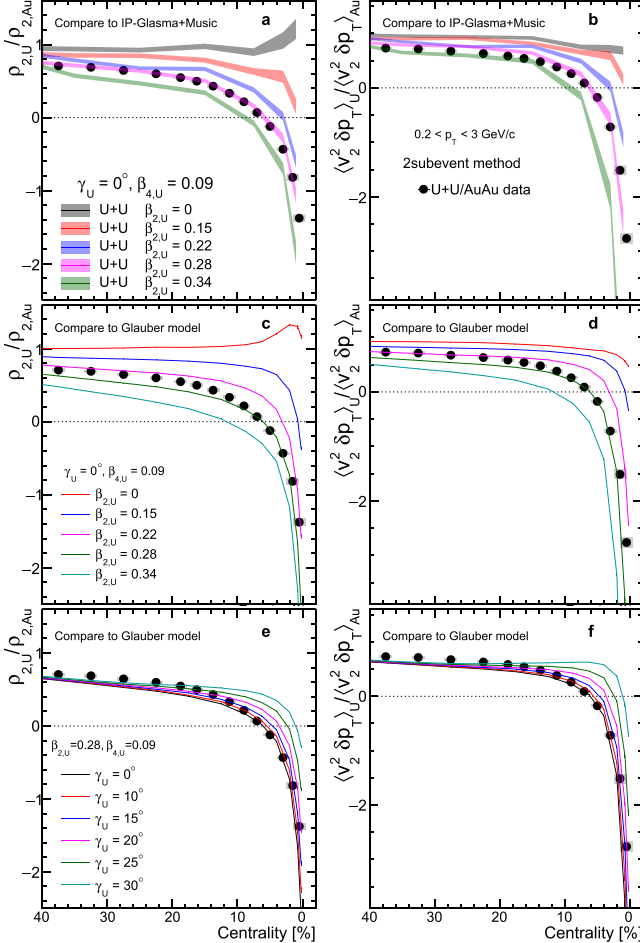


Figure 19. Ratios of ρ_2 (left panels) and $\langle v_2^2 \delta p_T \rangle$ (right panels) between U+U and Au+Au collisions, compared with the IP-Glasma+MUSIC (top row) and the Glauber model (middle row) with $\gamma_U = 0^\circ$ and different β_{2U} values, and Glauber model with $\beta_{2U} = 0.28$ and different γ_U and γ_{Au} (bottom row). In all cases, Au deformation parameters are fixed at $(\beta_{2Au}, \gamma_{Au}) = (0.14, 45^\circ)$, and $\beta_{4U} = 0.09$, except in middle row where $\beta_{4U} = 0$ (dashed lines) are also shown.

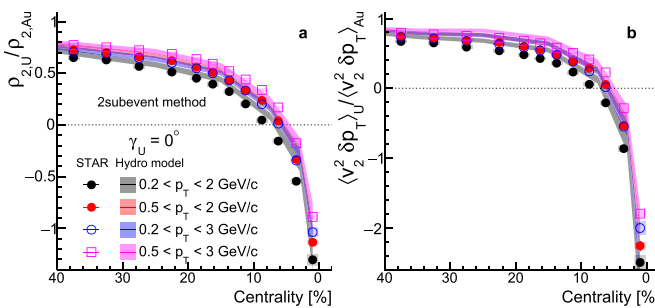


Figure 20. Ratio of ρ_2 (left) and $\langle v_2^2 \delta p_T \rangle$ (right) between U+U and Au+Au collisions in four p_T intervals, compared with hydrodynamic model predictions. Data in the UCC region have been rebinned for better comparison with the model.

0.28 and 0.34 are very close, but slightly lower than data for $\rho_2^{pcc,sub}$. Furthermore, the model values slightly increase with β_{4U} .

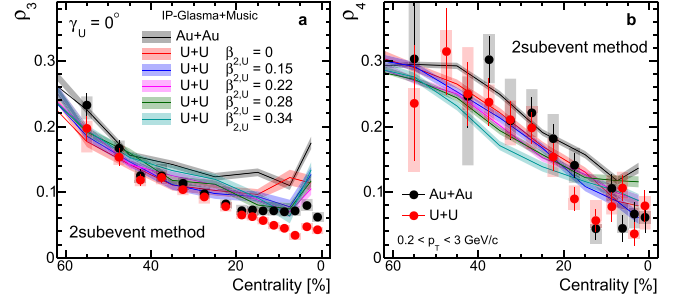


Figure 21. Centrality dependence of ρ_3 (left) and ρ_4 (right) from U+U and Au+Au collisions in $0.2 < p_T < 3 \text{ GeV c}^{-1}$, compared with hydrodynamic model predictions.

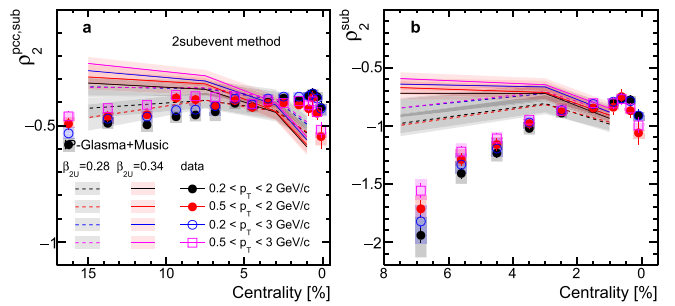


Figure 22. Centrality dependence of $\rho_2^{pcc,sub}$ (left) and ρ_2^{sub} (right) defined via equation (11) in four p_T ranges, compared with IP-Glasma+MUSIC calculations with $\gamma_U = 0^\circ$ and $\beta_{2U} = 0.28$ (dashed lines) and $\beta_{2U} = 0.34$ (solid lines).

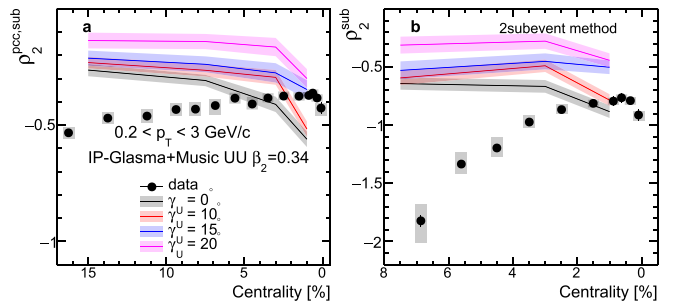


Figure 23. Centrality dependence of $\rho_2^{pcc,sub}$ (left) and ρ_2^{sub} (right) defined via equation (11). Compared with IP-Glasma+MUSIC calculations for $\beta_{2U} = 0.34$ and four γ_U values.

Bottom panels of figure 24 show the effect of varying γ_U with β_{2U} fixed at 0.28. Larger γ_U increases $\rho_2^{pcc,sub}$ and ρ_2^{sub} , with $\gamma_U = 15^\circ$ achieving the best agreement with data in the ultra-central region.

Role of β_{2U} and γ_U in UCCs. Data in the UCC region demonstrate the strongest sensitivity to nuclear deformation. Figure 25 show the β_{2U}^3 dependence of $R_{v_2^2 \delta p_T}$ in 0%–2% and 0%–5% centrality bins across four p_T intervals. Note that the influence of deformation is stronger in 0%–2% centrality, while the wider 0%–5% interval reduces centrality smearing effects. Experimental data are plotted at $\beta_{2,U}^3 = 0.022$ and compared with model calculations. IP-Glasma+MUSIC

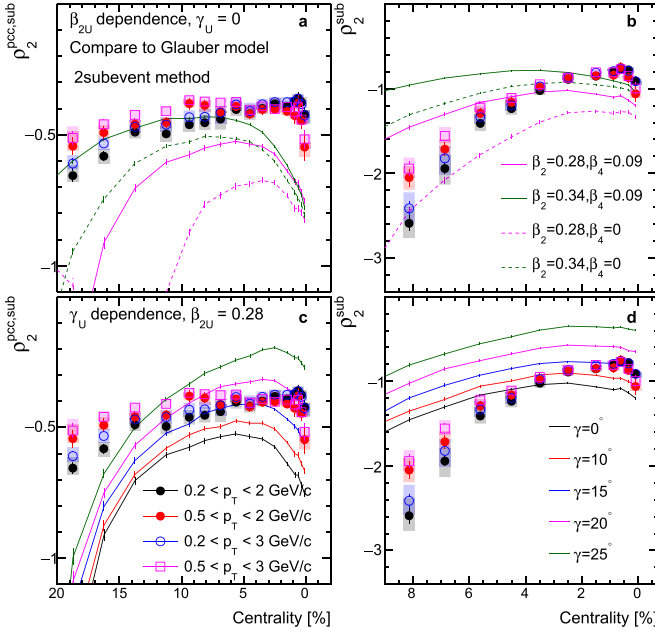


Figure 24. Centrality dependence of $\rho_2^{\text{pcc},\text{sub}}$ (left column) and ρ_2^{sub} (right column) via equation (11) in four p_T intervals. Compared with the Glauber model calculations for $\beta_{2U} = 0.28$ and 0.34 and $\beta_{4U} = 0$ and 0.09 (top panels) and $\beta_{2U} = 0.28$ and $\beta_{4U} = 0.09$ with different γ_U values (bottom panels). Glauber model calculations have no p_T dependence by construction.

predictions confirm a nearly linear dependence on β_2^3 , consistent with equation (2). Matching data to the model yields average values of $\beta_{2U} \approx 0.272$ – 0.289 (0%–2% centrality) and $\beta_{2U} \approx 0.291$ – 0.306 (0%–5% centrality) for $\gamma_U = 0^\circ$.

The negative data values in figure 25 require a positive $\cos(3\gamma)$, implying $\gamma_U < 30^\circ$. Since the Glauber model shows similar agreement to the full hydrodynamic model for $R_{v_2^2 \delta p_T}$, it can provide high-precision estimates of β_{2U} and γ_U . Right panels of figure 25 compared the β_2^3 dependence of $R_{v_2^2 \delta p_T}$ data with Glauber model's prediction for different γ_U values. The calculations exhibit a linear dependence on β_2^3 , independent of the γ . As the Glauber model does not simulate p_T dependence, we can only extract a broad constraint on γ_U . The extracted values are $\gamma_U \lesssim 17^\circ$ (0%–2% centrality) and $\gamma_U \lesssim 13^\circ$ (0%–5% centrality) assuming $\beta_{2U} = 0.28$.

The ratio of ρ_2 can also constrain nuclear deformation. However, this observable does not have a simple linear dependence on $\cos(3\gamma)\beta_2^3$ (figure 26), due to additional β_2^3 dependence introduced by $\langle v_2^2 \rangle$ and $\langle v_2^2 \delta p_T \rangle$ in the denominator of ρ_2 (see equation (13)). Therefore, the ratio of ρ_2 is not as robust for extracting nuclear deformations.

4.2. Quantitative constraints on Uranium deformation parameters

Having explored nuclear deformation's influence on flow observables and established that U+U to Au+Au ratios exhibit the clearest signatures of deformation, we now perform a more quantitative, simultaneous extraction of β_{2U} and γ_U . This is accomplished by using three observables $R_{v_2^2}$, $R_{(\delta p_T)^2}$,

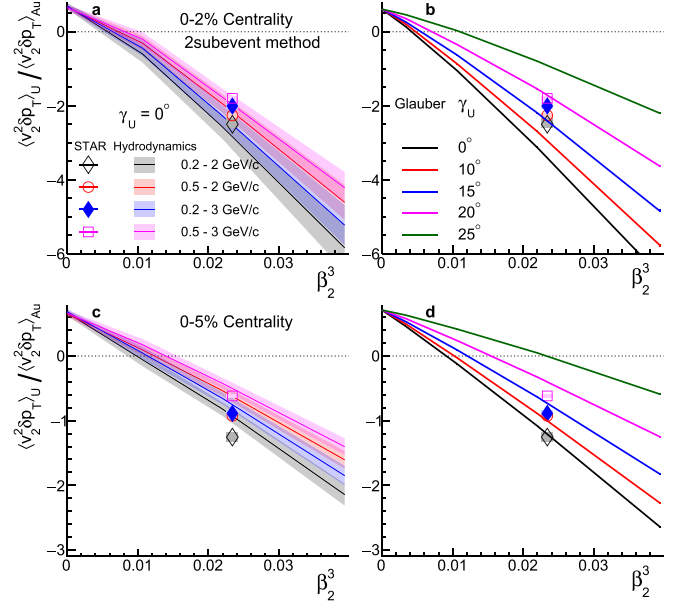


Figure 25. Ratio of covariance $\langle v_2^2 \delta p_T \rangle_{\text{UU}} / \langle v_2^2 \delta p_T \rangle_{\text{AuAu}}$ measured in 0%–2% (top row) and 0%–5% (bottom row) most central collisions for four p_T intervals, placed at $\beta_{2,U}^3 = 0.28^3 = 0.022$. Data are compared with the hydrodynamic model assuming $\gamma_U = 0$ (left column) and the Glauber model with different γ_U (right column). Uncertainties in the hydrodynamic model are correlated between different p_T intervals.

and $R_{v_2^2 \delta p_T}$ together. If we ignore the modest deformation in the Au nucleus, equation (2) suggests:

$$\begin{aligned} R_{v_2^2} &\approx \frac{a_{1,\text{U}}}{a_{1,\text{Au}}} \left(1 + \frac{b_1}{a_1} \beta_2^2 \right)_{\text{U}}, \\ R_{(\delta p_T)^2} &\approx \frac{a_{2,\text{U}}}{a_{2,\text{Au}}} \left(1 + \frac{b_2}{a_2} \beta_2^2 \right)_{\text{U}}, \\ R_{v_2^2 \delta p_T} &\approx \frac{a_{3,\text{U}}}{a_{3,\text{Au}}} \left(1 - \frac{b_3}{a_3} \beta_2^3 \cos(3\gamma) \right)_{\text{U}} \end{aligned} \quad (18)$$

In the absence of deformation, these ratios approach $a_{n,\text{U}}/a_{n,\text{Au}}$, which are less than unity in UCC where a_n are dominated by random fluctuations and are larger in Au+Au collisions. Following [16], we consider additional uncertainties for these ratios:

- **Non-flow estimate:** non-flow estimates, representing physical correlations, are included in the measured data ratios as model-dependent contributions (see section 2.3).
- **Impact of viscosity:** varying QGP shear and bulk viscosities by ±50% in IP-Glasma+MUSIC shows that while individual flow observables can change significantly, their ratios in U+U and Au+Au remain relatively stable (top panels of figure 27). Half the maximum variation is included in the model uncertainty.
- **Impact of other structure parameters:** to derive uncertainties on β_{2U} and γ_U , other Woods-Saxon inputs in table 1 are varied: (1) Au deformation parameters are varied within $\beta_{2\text{Au}} \approx 0.12$ – 0.14 and $\gamma_{\text{Au}} \approx 37$ – 53° according to [29, 30]. (2) The role of high-order deformation is checked by varying

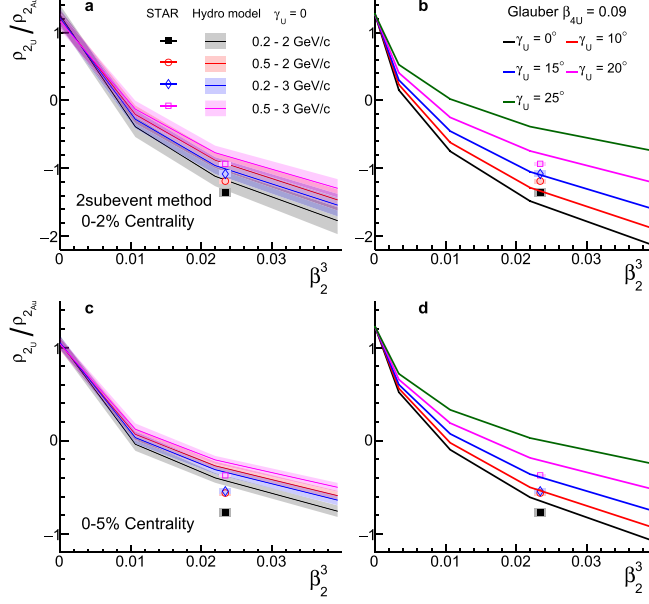


Figure 26. Ratio of covariance $\rho_{2,UU}/\rho_{2,AuAu}$ measured in 0%–2% (top row) and 0%–5% (bottom row) most central collisions for four p_T intervals, placed at $\beta_{2,U}^3 = 0.28^3 = 0.022$. Data are compared with the hydrodynamics model assuming $\gamma_U = 0$ (left column) and the Glauber model with different γ_U (right column). Due to oversampling, statistical uncertainties in the model are dominated by fluctuations in initial configurations and are therefore correlated across different p_T intervals.

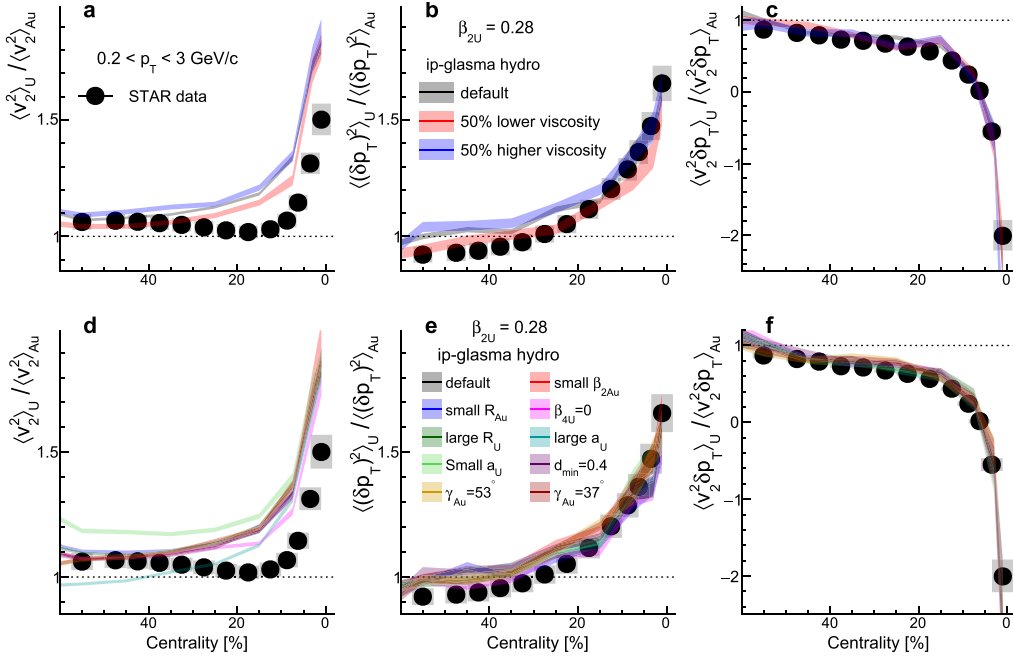


Figure 27. IP-Glasma+MUSIC model prediction of the ratios of $\langle v_2^2 \rangle$ (left column), $\langle (\delta p_T)^2 \rangle$ (middle column), and $\langle v_2^2 \delta p_T \rangle$ (right column) between U+U and Au+Au collisions in $0.2 < p_T < 3 \text{ GeV } c^{-1}$, calculated for varying shear and bulk viscosities (top row) and varying nuclear structure parameters (bottom row), compared with the data. Checks consistent with the default calculation within their statistical uncertainties are not included in the model uncertainties in figure 28.

β_{4U} from 0 to 0.09. (3) The assumed nuclear radius R_0 and nuclear skin a are varied. (4) Parameters common to both collision systems, like the minimum inter-nucleon distance in nuclei d_{\min} are also varied. The impact of these variations on ratios of flow observables is shown in the bottom panels of figure 27. Dependencies on these structural parameters are small in the most central collisions.

Figure 27 shows that IP-Glasma+MUSIC generally matches central data for $R_{(\delta p_T)^2}$ and $R_{v_2^2 \delta p_T}$ but consistently overestimates $R_{v_2^2}$ in 0%–30% centrality. This overestimation for $R_{v_2^2}$ may stem from a stronger sensitivity to centrality smearing, other structural parameters (such as nuclear radius and skin depth) [74], and possible longitudinal flow decorrelations [79]. Thus, $R_{v_2^2}$ comparison

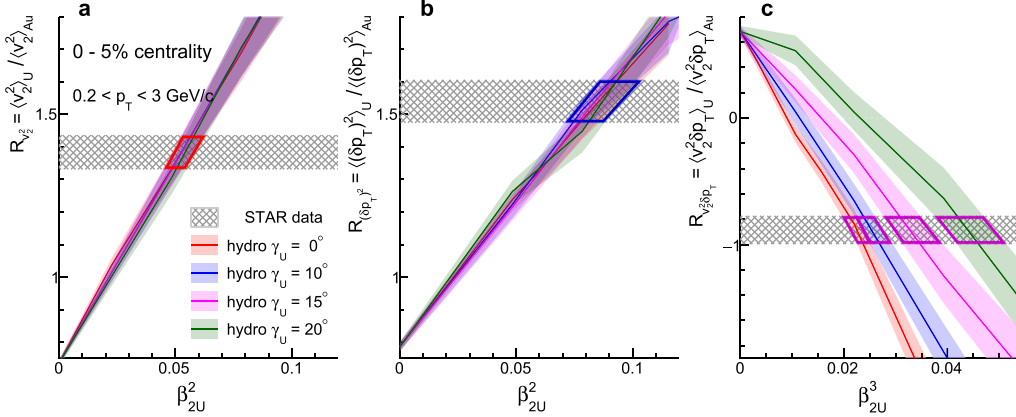


Figure 28. Ratio values in 0%–5% most central collisions for $0.2 < p_T < 3 \text{ GeV c}^{-1}$ (hatch bands) for $\langle v_2^2 \rangle$ (a), $\langle (\delta p_T)^2 \rangle$ (b), and $\langle v_2^2 \delta p_T \rangle$ (c) are compared with model calculations as a function of β_{2U}^2 or β_{2U}^3 for four γ_U values. Colored quadrilaterals delineate the allowed ranges of β_{2U}^2 or β_{2U}^3 from this data-model comparison.

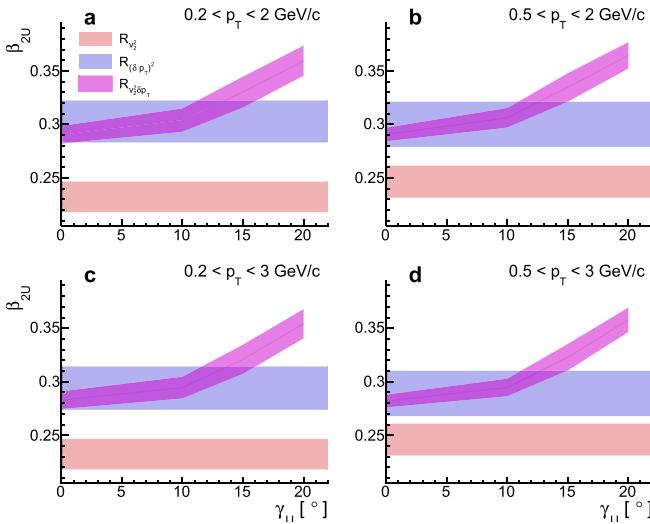


Figure 29. Constraints on β_{2U} and γ_U from the three ratios, obtained for four p_T ranges.

is considered to set a lower bound for β_{2U} in this model.

To minimize various confounding geometry effects, we focus on 0%–5% UCCs, where deformation signals dominate. Figure 28 compares the 0.2–3 GeV c^{-1} data with IP-Glasma+MUSIC curves, generated by varying β_{2U} (0 to 0.34) and γ_U (0° to 20°). Model uncertainties incorporate both final-state viscosities and initial-parameter scans are shown in figure 27. Calculated $R_{v_2^2}$ and $R_{(\delta p_T)^2}$ change linearly with β_{2U}^2 , while $R_{v_2^2 \delta p_T}$ follows a $\beta_{2U}^3 \cos(3\gamma_U)$ trend, remarkably consistent with equation (18)¹. Intersections between data and model delineate the preferred ranges of β_{2U} . For $R_{v_2^2 \delta p_T}$, the favored β_{2U} range varies with γ_U .

¹ However, the predicted $R_{(\delta p_T)^2}$ values display a small dependence on γ_U when $\gamma_U > 30^\circ$.

We repeat this comparison for all four p_T intervals. Figure 29 shows the extracted best-fit regions of (β_{2U}, γ_U) . $R_{v_2^2}$ sets the lower bound of β_{2U} , while $R_{(\delta p_T)^2}$ and $R_{v_2^2 \delta p_T}$ further constrain the upper range and triaxiality. A pseudo-experiment procedure combines uncertainties from $R_{(\delta p_T)^2}$ and $R_{v_2^2 \delta p_T}$, assuming independent Gaussian probability density functions:

$$P(\beta_{2U}, \gamma_U) \propto \exp \left(-\frac{(\beta_{2U} - \bar{\beta}_a)^2}{2\sigma_a^2} - \frac{(\beta_{2U} - \bar{\beta}_b(\gamma_U))^2}{2\sigma_b^2(\gamma_U)} \right). \quad (19)$$

Here, $\bar{\beta}_a$ and σ_a are the mean and uncertainty of β_{2U} extracted from $R_{(\delta p_T)^2}$. Similarly, $\bar{\beta}_b$ and σ_b are the mean and uncertainty of β_{2U} from $R_{v_2^2 \delta p_T}$, and they depend on γ_U . We sample a uniform prior distribution in β_{2U} and γ_U to obtain the posterior distribution, from which we obtained the mean and one standard deviation uncertainty of β_{2U} and γ_U .

The constraints are listed in table 2 for the four p_T intervals. Averaging across these p_T windows, we find $\beta_{2U} \approx 0.300 \pm 0.016$ and $\gamma_U \approx 8.3 \pm 4.7^\circ$ from $R_{(\delta p_T)^2}$ and $R_{v_2^2 \delta p_T}$. In contrast, $R_{v_2^2}$ alone provides a lower-limit estimate of $\beta_{2U} \approx 0.24 \pm 0.02$. This finding is consistent with recent model studies [29, 80], where $\beta_{2U} \sim 0.25$ could describe $R_{v_2^2}$ data. Similar nuclear structure constraints have also reported using a different hydrodynamic model framework [48, 49].

We caution that shape parameters are extracted within the Woods–Saxon parametrization, where deformation values are defined at the nuclear surface. In the low-energy community, β_2 from the spectroscopic method corresponds to a β_2 defined using the body distribution of the nucleons [29]. In the presence of a positive β_4 , the β_2 value from Woods–Saxon parametrization can be slightly reduced compared to the actual β_2 for the body deformation [81]. Therefore, it is valuable to derive an independent constraint on the β_4 from high-energy collisions, which should be explored in the future.

Another point is worth mentioning. In [16], an independent estimate of β_{2U} and γ_U was obtained from another hydrodynamic model, Trajectum [82]. Their reported values, $(\beta_{2U}, \gamma_U) = (0.286 \pm 0.025, 8.7^\circ \pm 4.5^\circ)$, are obtained for one

Table 2. One standard deviation constraint on the uranium shape parameters from the three ratios in 0%–5% centrality for four p_T intervals. Results averaged over the four p_T ranges are also displayed.

p_T range (GeV c $^{-1}$)	$R_{(\delta p_T)^2}$ and $R_{v_2^2 \delta p_T}$ combined $\beta_{2U}, \gamma_U (^\circ)$	$R_{v_2^2}$ β_{2U}
0.2–2	$0.305 \pm 0.014, 8.6 \pm 4.8$	0.232 ± 0.014
0.5–2	$0.305 \pm 0.014, 8.2 \pm 4.6$	0.247 ± 0.017
0.2–3	$0.297 \pm 0.014, 8.5 \pm 4.8$	0.234 ± 0.014
0.5–3	$0.296 \pm 0.013, 8.1 \pm 4.6$	0.246 ± 0.017
Combined	$0.300 \pm 0.016, 8.3 \pm 4.7$	0.240 ± 0.018

p_T bin, by combining the two constraints and including the model differences as additional uncertainties, and hence are not the same as what is reported in this analysis.

Overall, the extracted deformation parameters align with low-energy nuclear measurements under the rigid-rotor assumption [25]. These constraints are achieved without referencing transitions to excited nuclear states, demonstrating how ultra-central high-energy collisions probe ground-state nuclear shapes.

5. Summary and outlook

The correlation between elliptic flow (v_2) and event-by-event average transverse momentum ($|p_T|$) in high-energy heavy-ion collisions offers a unique probe to the shape of the colliding nuclei, notably their quadrupole deformation (β_2) and triaxiality (γ). This sensitivity is robustly demonstrated by comparing collisions of strong prolate-deformed ^{238}U nuclei with weakly oblate-deformed ^{197}Au nuclei, focusing on three observables: $\langle v_2^2 \rangle$, $\langle (\delta p_T)^2 \rangle$, and $\langle v_2^2 \delta p_T \rangle$.

We construct a normalized quantity, $\rho_2 = \frac{\langle v_2^2 \delta p_T \rangle}{\langle v_2^2 \rangle \sqrt{\langle (\delta p_T)^2 \rangle}}$, which reduces sensitivity to final-state expansion dynamics. In 0%–7% ultra-central U+U collisions, ρ_2 exhibits a steep transition from positive to negative values, whereas it stays nearly constant in Au+Au collisions. Further suppression of residual final-state effects is achieved by using the ratio $R_{v_2^2 \delta p_T} = \langle v_2^2 \delta p_T \rangle_{\text{U}} / \langle v_2^2 \delta p_T \rangle_{\text{Au}}$. This ratio shows a sharp decrease in central collisions, nearly independent of the correlation methods or p_T selections. This provides direct evidence from the high-energy regime that ^{238}U possesses strong prolate deformation (large β_{2U}) and small triaxiality ($\gamma_U \sim 0^\circ$). Independent evidence for large β_{2U} also comes from the strong rise of $R_{v_2^2} = \langle v_2^2 \rangle_{\text{U}} / \langle v_2^2 \rangle_{\text{Au}}$ and $R_{(\delta p_T)^2} = \langle ((\delta p_T)^2) \rangle_{\text{U}} / \langle ((\delta p_T)^2) \rangle_{\text{Au}}$ in UCCs. In contrast, observables associated with higher-order harmonics (v_3 and v_4), which are less affected by quadrupole deformation, show much smaller differences between U+U and Au+Au systems.

The $\langle v_2^2 \delta p_T \rangle$ data were compared with both a Glauber model, which accounts for the influence of nuclear deformation on initial collision conditions, and a state-of-the-art hydrodynamic model simulation (IP-Glasma+MUSIC), which incorporates final-state effects. Both models employ the Woods-Saxon parameterization for nuclear deformation.

These models quantitatively reproduce the centrality dependence of $R_{v_2^2 \delta p_T}$ when $\beta_{2U} = 0.28$ and $\gamma_U = 0^\circ$. In UCCs, where deformation effects are dominant, the IP-Glasma+MUSIC model yields $\beta_{2U} \approx 0.27$ –0.30, while the Glauber model supports a triaxiality value of $\gamma_U \lesssim 15^\circ$.

For a more precise extraction of the uranium shape, we performed a joint fit of the hydrodynamic model to both $R_{(\delta p_T)^2}$ data (mainly constraining β_{2U}) and $R_{v_2^2 \delta p_T}$ data (sensitive to both β_{2U} and γ_U). By accounting for variations in medium evolution and initial-state parameters, and incorporating non-flow effects in the data, we determine $\beta_{2U} = 0.300 \pm 0.016$ and $\gamma_U = 8.3 \pm 4.7^\circ$. These values are broadly consistent with low-energy estimates under the rigid-rotor assumption. This marks a valuable extraction of the nuclear ground-state shape purely from high-energy collisions.

Observables involving higher-order flow harmonics, such as $\langle v_3^2 \rangle$, $\langle v_4^2 \rangle$, $\langle v_3^2 \delta p_T \rangle$ and $\langle v_4^2 \delta p_T \rangle$, are also sensitive to octupole β_3 and hexadecapole β_4 deformations. Our findings that $\langle v_3^2 \rangle_{\text{U}} / \langle v_3^2 \rangle_{\text{Au}} > 1$ and $\langle v_3^2 \delta p_T \rangle_{\text{U}} / \langle v_3^2 \delta p_T \rangle_{\text{Au}} < 1$ in UCCs are consistent with the presence of a modest $\beta_{3U} \sim 0.08$ –0.10 [36]. This represents the first experimental evidence from the high-energy regime for octupole collectivity of ^{238}U . While a similar analysis was performed for β_{4U} , the uncertainties in analogous ratios involving $\langle v_4^2 \rangle$ and $\langle v_4^2 \delta p_T \rangle$ were too large for a definite statement.

The successful application of imaging nuclear shapes via high-energy heavy-ion collisions raises questions about the relationship between these short-timescale snapshot measurements (where the collision crossing time is $\lesssim 0.1 \text{ fm c}^{-1}$) and traditional low-energy methods, which probe much longer timescales. This approach also raises issues about possible partonic modifications within highly boosted nuclei. Addressing these questions is crucial for advancing our understanding of the elusive initial state of heavy-ion collisions. Further studies, incorporating various hydrodynamic modeling frameworks and an explicit treatment of longitudinal decorrelations, are necessary to refine this imaging technique. This is particularly important in small collision systems, where uncertainties in the properties and initial conditions of the QGP could reduce the sensitivity to nuclear structure differences between isobar-like species.

To establish the ‘imaging-by-smashing’ method as a potential discovery tool, it must first be calibrated using isobar nuclei with known shapes. This calibration allows for the tuning of key response coefficients (equations (2) and (3)) within the theoretical models used for analysis. The method must then be

validated with additional species with known nuclear shapes to cross-check these coefficients and expose any limitations or inconsistencies [31]. Furthermore, uncertainty quantification must account for model dependencies inherent in shape parameters derived from low-energy experiments [83]. These calibration and validation steps are also crucial for placing stricter constraints on the initial conditions, dynamics, and properties of the QGP. With proper validation, this imaging method can become a complementary tool for studying the collective, many-body structure of atomic nuclei across the nuclide chart and at various energy scales. This goal can be achieved by leveraging collider and fixed-target facilities to collide carefully selected isobar species [14].

The STAR Collaboration

B E Aboona⁵⁸, J Adam¹⁷, G Agakishiev³², I Aggarwal⁴⁴, M M Aggarwal⁴⁴, Z Ahammed⁶⁵, A Aitbayev³², I Alekseev^{3,40}, E Alpatov⁴⁰, A K Alshammri³³, A Aparin³², S Aslam²¹, J Atchison², G S Averichev³², V Bairathi⁵⁶, X Bao⁵², K Barish¹², S Behera²⁷, P Bhagat³¹, A Bhasin³¹, S Bhatta⁵⁵, I G Bordyuzhin³, J D Brandenburg⁴³, A V Brandin⁴⁰, C Broodo²⁴, X Z Cai⁵³, H Caines⁶⁹, M Calderón de la Barca Sánchez¹⁰, D Cebra¹⁰, J Ceska¹⁷, I Chakaberia³⁶, Y S Chang⁴⁶, Z Chang²⁹, A Chatterjee¹⁸, D Chen¹², J H Chen²¹, Q Chen²², W Chen²¹, Z Chen⁵², J Cheng⁶¹, Y Cheng¹¹, W Christie⁷, X Chu⁷, S Corey⁴³, H J Crawford⁹, G Dale-Gau¹⁴, A Das¹⁷, T G Dedovich³², I M Deppner²³, A A Derevschikov⁴⁵, A Deshpande⁵⁵, A Dhamija⁴⁴, A Dimri⁵⁵, P Dixit²⁶, X Dong³⁶, J L Drachenberg², E Duckworth³³, J C Dunlop⁷, J Engelage⁹, G Eppley⁴⁷, S Esumi⁶², O Evdokimov¹⁴, O Eyser⁷, B Fan¹³, R Fatemi³⁴, S Fazio⁸, Y Feng⁴⁶, E Finch⁵⁴, Y Fisyak⁷, F A Flor⁶⁹, C Fu³⁰, T Fu⁵², T Gao⁵², Y Gao²¹, F Geurts⁴⁷, A Gibson⁶⁴, K Gopal²⁷, X Gou⁵², D Grosnick⁶⁴, A Gu²⁵, A Gupta³¹, A Hamed⁵, R J Hamilton⁶⁹, X Han⁴³, M D Harasty¹⁰, J W Harris⁶⁹, H Harrison-Smith³⁴, L B Havener⁶⁹, X H He³⁰, Y He⁵², C Hu⁶³, Q Hu³⁰, Y Hu³⁶, H Huang^{42,1}, H Z Huang¹¹, S L Huang⁵⁵, T Huang¹⁴, Y Huang¹⁹, Y Huang¹³, Y Huang²¹, M Isshiki⁶², W W Jacobs²⁹, A Jalotra³¹, C Jena²⁷, Y Ji³⁶, J Jia^{55,7,*}, X Jiang¹³, C Jin⁴⁷, Y Jin¹³, N Jindal⁴³, X Ju⁴⁹, E G Judd⁹, S Kabana⁵⁶, D Kalinkin³⁴, K Kang⁶¹, D Kapukchyan¹², K Kauder⁷, D Keane³³, A Kechechyan³², M Kesler³³, A Khanal⁶⁷, J Kim⁷, A Kiselev⁷, A G Knospe³⁷, L Kochenda⁴⁰, A A Korobitsin³², B Korodi⁴³, A Yu Kraeva⁴⁰, P Kravtsov⁴⁰, L Kumar⁴⁴, M C Labonte¹⁰, R Lacey⁵⁵, J M Landgraf⁷, C Larson³⁴, A Lebedev⁷, R Lednicky³², J H Lee⁷, Y H Leung²³, D Li⁴⁹, H-S Li⁴⁶, H Li⁶⁸, H Li²², H Li¹³, W Li⁴⁷, X Li⁴⁹, X Li⁴⁹, Y Li⁶¹, Z Li⁵⁰, Z Li⁴⁹, X Liang¹², T Lin⁵², Y Lin²², C Liu³⁰, G Liu⁵⁰, H Liu²⁵, L Liu¹³, L Liu²¹, Z Liu²¹, Z Liu¹³, T Ljubicic⁴⁷, O Lomicky¹⁷, E M Loyd¹², T Lu³⁰, J Luo⁴⁹, X F Luo¹³, V B Luong³², Ma²¹, R Ma⁷, Y G Ma²¹, N Magdy⁵⁹, R Manikandhan²⁴, S Margetis³³, O Matonoha¹⁷, K Mi⁶³, N G Minaev⁴⁵, B Mohanty⁴¹, B Mondal⁴¹, M M Mondal⁴¹, I Mooney⁶⁹, D A Morozov⁴⁵, M I Nagy¹⁹, C J Naim⁵⁵, A S Nain⁴⁴, J D Nam⁵⁷, M Nasim²⁶, H Nasrulloh⁴⁹, E Nedorezov³², J M Nelson⁹, M Nie⁵², G Nigmatkulov¹⁴, T

Niida⁶², L V Nogach⁴⁵, T Nonaka⁶², G Odyniec³⁶, A Ogawa⁷, S Oh⁵¹, V A Okorokov⁴⁰, K Okubo⁶², B S Page⁷, S Pal¹⁷, A Pandav³⁶, A Panday²⁶, A K Pandey⁶⁶, Y Panebratsev³², T Pani⁴⁸, P Parfenov⁴⁰, A Paul¹², S Paul⁵⁵, C Perkins⁹, S Ping²¹, B R Pokhrel⁵⁷, I D Ponce Pinto⁶⁹, M Posik⁵⁷, E Pottebaum⁶⁹, A Povarov⁴⁰, S Prodhan²⁷, T L Protzman³⁷, N K Pruthi⁴⁴, J Putschke⁶⁷, Z Qin⁶¹, H Qiu³⁰, C Racz¹², S K Radhakrishnan³³, A Rana⁴⁴, R L Ray⁶⁰, C W Robertson⁴⁶, O V Rogachevsky³², M A Rosales Aguilar³⁴, D Roy⁴⁸, L Ruan⁷, A K Sahoo²⁶, N R Sahoo²⁷, H Sako⁶², S Salur⁴⁸, S S Sambyal³¹, E Samigullin³, J K Sandhu³⁷, S Sato⁶², B C Schaefer³⁷, N Schmitz³⁸, J Seger¹⁶, R Seto¹², P Seyboth³⁸, N Shah²⁸, E Shahaliev³², P V Shanmuganathan⁷, T Shao²¹, M Sharma³¹, N Sharma²⁶, R Sharma²⁷, S R Sharma²⁷, A I Sheikh³³, D Shen⁵², D Y Shen³⁰, K Shen⁴⁹, S Shi¹³, Y Shi⁵², F Si⁴⁹, J Singh⁵⁶, S Singha³⁰, P Sinha²⁷, M J Skoby^{6,46}, Y Söhngen²³, Y Song⁶⁹, T D S Stanislaus⁶⁴, M Strikhanov⁴⁰, Y Su⁴⁹, X Sun³⁰, Y Sun⁴⁹, B Surrow⁵⁷, D N Svirida³, Z W Sweger¹⁰, A C Tamis⁶⁹, A H Tang⁷, Z Tang⁴⁹, A Tarantenko⁴⁰, T Tarnowsky³⁹, J H Thomas³⁶, A Timofeev³², D Tlusty¹⁶, M V Tokarev³², D Torres Valladares⁴⁷, S Trentalange¹¹, P Tribedy⁷, O D Tsai^{11,7}, C Y Tsang^{33,7}, Z Tu⁷, J E Tyler⁵⁸, T Ullrich⁷, D G Underwood^{4,64}, G Van Buren⁷, A N Vasiliev^{45,40}, F Videbæk⁷, S Vokal³², S A Voloshin⁶⁷, G Wang¹¹, G Wang¹³, J S Wang²⁵, J Wang⁵², K Wang⁴⁹, X Wang⁵², Y Wang⁴⁹, Y Wang¹³, Y Wang⁶¹, Z Wang²¹, Z Wang⁵², J C Webb⁷, P C Weidenkaff²³, G D Westfall³⁹, H Wieman³⁶, G Wilks¹⁴, S W Wissink²⁹, C P Wong⁷, J Wu⁶³, X Wu¹¹, X Wu⁴⁹, X Wu¹³, B Xi²¹, Y Xiao²¹, Z G Xiao⁶¹, G Xie⁶³, W Xie⁴⁶, H Xu²⁵, N Xu¹³, Q H Xu⁵², Y Xu⁵², Y Xu²¹, Y Xu¹³, Y Xu³⁰, Z Xu³³, Z Xu⁴, G Yan⁵², Z Yan⁵⁵, C Yang⁵², Q Yang⁵², S Yang⁵⁰, Y Yang^{1,42}, Z Ye⁵⁰, Z Ye³⁶, L Yi⁵², Y Yu⁵², W Zha⁴⁹, C Zhang²¹, D Zhang⁵⁰, J Zhang⁵², L Zhang¹³, S Zhang¹⁵, W Zhang⁵⁰, X Zhang³⁰, Y Zhang³⁰, Y Zhang⁴⁹, Y Zhang⁵², Y Zhang²², Z Zhang⁷, Z Zhang¹⁴, F Zhao³⁵, J Zhao²¹, S Zhou¹³, Y Zhou¹³, X Zhu⁶¹, M Zurek^{4,7}, M Zyzak²⁰

¹Academia Sinica, Nankang 115, Taiwan

²Abilene Christian University, Abilene, TX 79699, United States of America

³Alikhanov Institute for Theoretical and Experimental Physics NRC ‘Kurchatov Institute’, Moscow 117218, Russia

⁴Argonne National Laboratory, Argonne, IL 60439, United States of America

⁵American University in Cairo, New Cairo 11835, Egypt

⁶Ball State University, Muncie, IN 47306, United States of America

⁷Brookhaven National Laboratory, Upton, NY 11973, United States of America

⁸University of Calabria & INFN-Cosenza, Rende 87036, Italy

⁹University of California, Berkeley, CA 94720, United States of America

¹⁰University of California, Davis, CA 95616, United States of America

¹¹University of California, Los Angeles, CA 90095, United States of America

¹²University of California, Riverside, CA 92521, United States of America

- ¹³Central China Normal University, Wuhan, Hubei 430079, People's Republic of China
- ¹⁴University of Illinois at Chicago, Chicago, IL 60607, United States of America
- ¹⁵Chongqing University, Chongqing 401331, People's Republic of China
- ¹⁶Creighton University, Omaha, NE 68178, United States of America
- ¹⁷Czech Technical University in Prague, FNSPE, Prague 115 19, Czech Republic
- ¹⁸National Institute of Technology Durgapur, Durgapur 713209, India
- ¹⁹ELTE Eötvös Loránd University, Budapest H-1117, Hungary
- ²⁰Frankfurt Institute for Advanced Studies FIAS, Frankfurt 60438, Germany
- ²¹Fudan University, Shanghai 200433, People's Republic of China
- ²²Guangxi Normal University, Guilin 541004, People's Republic of China
- ²³University of Heidelberg, Heidelberg 69120, Germany
- ²⁴University of Houston, Houston, TX 77204, United States of America
- ²⁵Huzhou University, Huzhou, Zhejiang 313000, People's Republic of China
- ²⁶Indian Institute of Science Education and Research (IISER), Berhampur 760010, India
- ²⁷Indian Institute of Science Education and Research (IISER) Tirupati, Tirupati 517507, India
- ²⁸Indian Institute of Technology, Patna, Bihar 801106, India
- ²⁹Indiana University, Bloomington, IN 47408, United States of America
- ³⁰Institute of Modern Physics, Chinese Academy of Sciences, Lanzhou, Gansu 730000, People's Republic of China
- ³¹University of Jammu, Jammu 180001, India
- ³²Joint Institute for Nuclear Research, Dubna 141 980, Russia
- ³³Kent State University, Kent, OH 44242, United States of America
- ³⁴University of Kentucky, Lexington, KY 40506-0055, United States of America
- ³⁵Lanzhou University, Lanzhou 730000, People's Republic of China
- ³⁶Lawrence Berkeley National Laboratory, Berkeley, CA 94720, United States of America
- ³⁷Lehigh University, Bethlehem, PA 18015, United States of America
- ³⁸Max-Planck-Institut für Physik, Munich 80805, Germany
- ³⁹Michigan State University, East Lansing, MI 48824, United States of America
- ⁴⁰National Research Nuclear University MEPhI, Moscow 115409, Russia
- ⁴¹National Institute of Science Education and Research, HBNI, Jatni 752050, India
- ⁴²National Cheng Kung University, Tainan 70101, Taiwan
- ⁴³The Ohio State University, Columbus, OH 43210, United States of America
- ⁴⁴Panjab University, Chandigarh 160014, India
- ⁴⁵NRC 'Kurchatov Institute', Institute of High Energy Physics, Protvino 142281, Russia
- ⁴⁶Purdue University, West Lafayette, IN 47907, United States of America
- ⁴⁷Rice University, Houston, TX 77251, United States of America
- ⁴⁸Rutgers University, Piscataway, NJ 08854, United States of America
- ⁴⁹University of Science and Technology of China, Hefei, Anhui 230026, People's Republic of China
- ⁵⁰South China Normal University, Guangzhou, Guangdong 510631, People's Republic of China
- ⁵¹Sejong University, Seoul 05006, Republic of Korea
- ⁵²Shandong University, Qingdao, Shandong 266237, People's Republic of China
- ⁵³Shanghai Institute of Applied Physics, Chinese Academy of Sciences, Shanghai 201800, People's Republic of China
- ⁵⁴Southern Connecticut State University, New Haven, CT 06515, United States of America
- ⁵⁵State University of New York, Stony Brook, NY 11794, United States of America
- ⁵⁶Instituto de Alta Investigación, Universidad de Tarapacá, Arica 1000000, Chile
- ⁵⁷Temple University, Philadelphia, PA 19122, United States of America
- ⁵⁸Texas A&M University, College Station, TX 77843, United States of America
- ⁵⁹Texas Southern University, Houston, TX 77004, United States of America
- ⁶⁰University of Texas, Austin, TX 78712, United States of America
- ⁶¹Tsinghua University, Beijing 100084, People's Republic of China
- ⁶²University of Tsukuba, Tsukuba, Ibaraki 305-8571, Japan
- ⁶³University of Chinese Academy of Sciences, Beijing, 101408, People's Republic of China
- ⁶⁴Valparaiso University, Valparaiso, IN 46383, United States of America
- ⁶⁵Variable Energy Cyclotron Centre, Kolkata 700064, India
- ⁶⁶Warsaw University of Technology, Warsaw 00-661, Poland
- ⁶⁷Wayne State University, Detroit, MI 48201, United States of America
- ⁶⁸Wuhan University of Science and Technology, Wuhan, Hubei 430065, People's Republic of China
- ⁶⁹Yale University, New Haven, CT 06520, United States of America

Data availability statement

All raw data for this study were collected using the STAR detector at Brookhaven National Laboratory and are not available to the public. Derived data supporting the findings of this study are publicly available in the HEPData repository (www.hepdata.net/record/159930) or from the corresponding author on request. The data that support the findings of this study are available upon reasonable request from the authors.

Acknowledgments

We thank Chun Shen for providing the IP-Glasma+MUSIC code. We thank the RHIC Operations Group and SDCC at BNL, the NERSC Center at LBNL, and the Open Science Grid consortium for providing resources and support. This work was supported in part by the Office of Nuclear Physics within the U.S. DOE Office of Science, the U.S. National Science Foundation, National Natural Science Foundation of China, Chinese Academy of Science, the Ministry of Science and Technology of China and the Chinese Ministry of Education, NSTC Taipei, the National Research Foundation of Korea, Czech Science Foundation and Ministry of Education, Youth and Sports of the Czech Republic, Hungarian National Research, Development and Innovation Office, New National Excellency Programme of the Hungarian Ministry of Human Capacities, Department of Atomic Energy and Department of Science and Technology of the Government of India, the National Science Centre and WUT ID-UB of Poland, the Ministry of Science,

Education and Sports of the Republic of Croatia, German Bundesministerium für Bildung, Wissenschaft, Forschung and Technologie (BMBF), Helmholtz Association, Ministry of Education, Culture, Sports, Science, and Technology (MEXT), and Japan Society for the Promotion of Science (JSPS).

Appendix. Comprehensive data plots

The results in the paper are mainly presented as a function of centrality. However, it is also helpful to present them as a function of N_{ch} for direct comparison with models. We collect the data for all observables used in this paper in U+U and Au+Au collisions, $\langle v_n^2 \rangle$, $\langle p_T \rangle$, $\langle (\delta p_T)^2 \rangle$, and $\langle v_n^2 \delta p_T \rangle$ for $n = 2, 3, 4$, and present them in figures 30–37 for four p_T ranges as a function of either centrality or N_{ch} . The ratios between the two collision systems as a function of centrality are shown in figure 38.

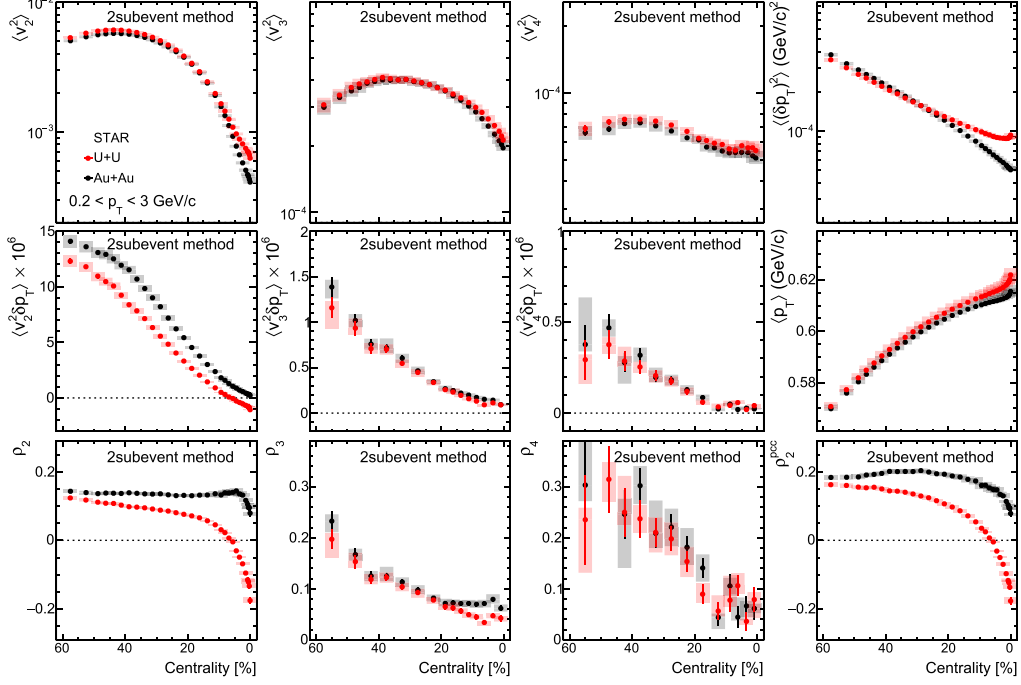


Figure 30. Observables as a function of centrality in U+U and Au+Au collisions for charged hadrons in $0.2 < p_T < 3 \text{ GeV c}^{-1}$.

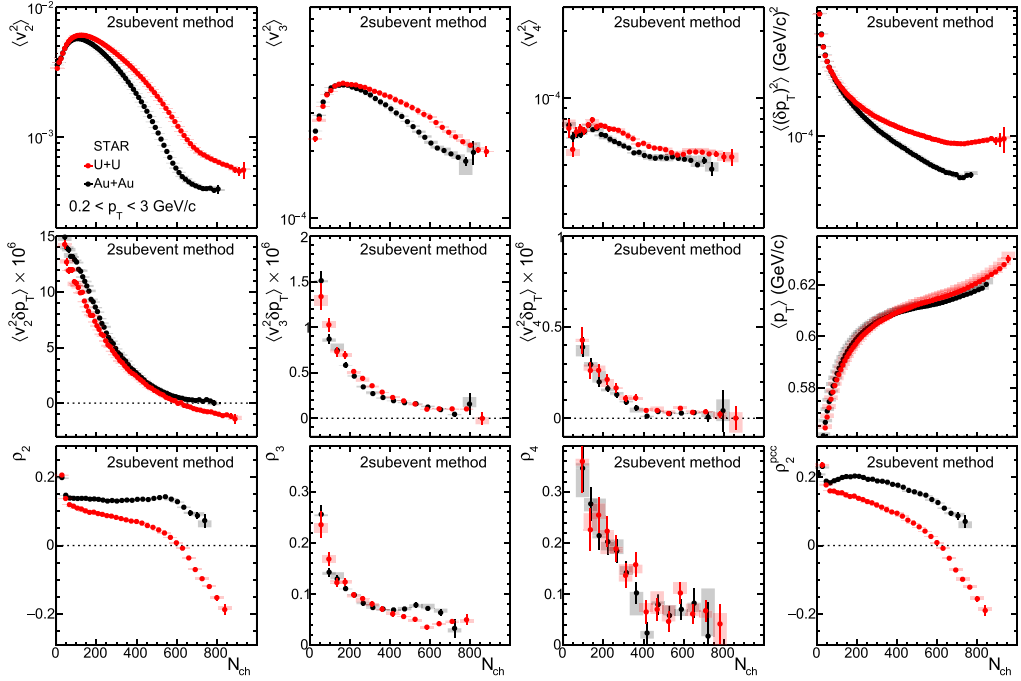


Figure 31. Observables as a function of N_{ch} in U+U and Au+Au collisions for charged hadrons in $0.2 < p_T < 3 \text{ GeV c}^{-1}$.

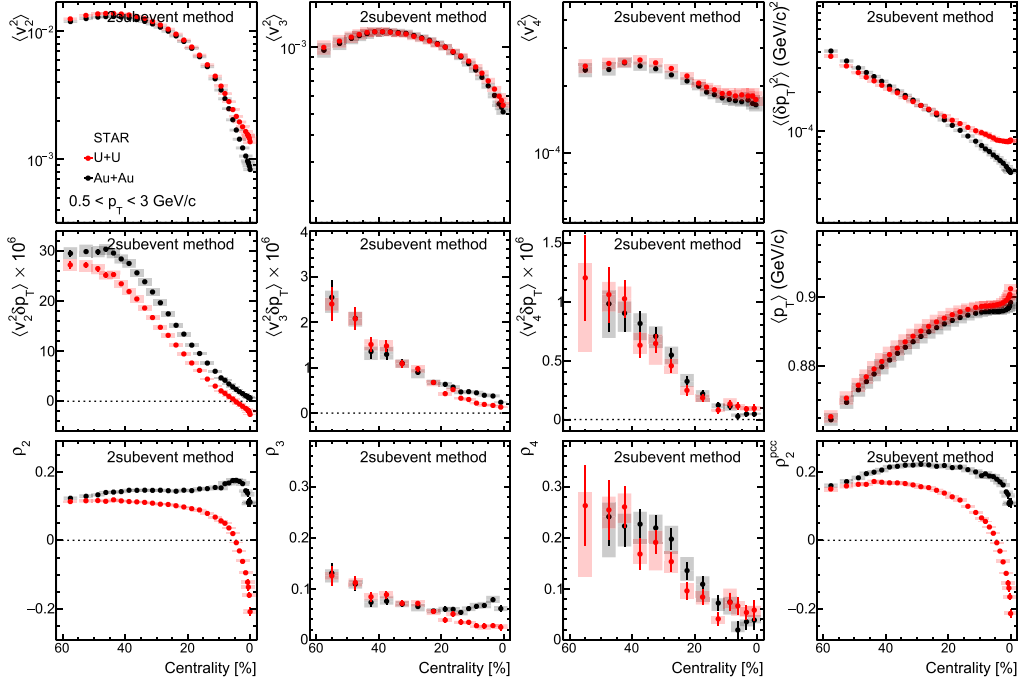


Figure 32. Observables as a function of centrality in U+U and Au+Au collisions for charged hadrons in $0.5 < p_T < 3 \text{ GeV c}^{-1}$.

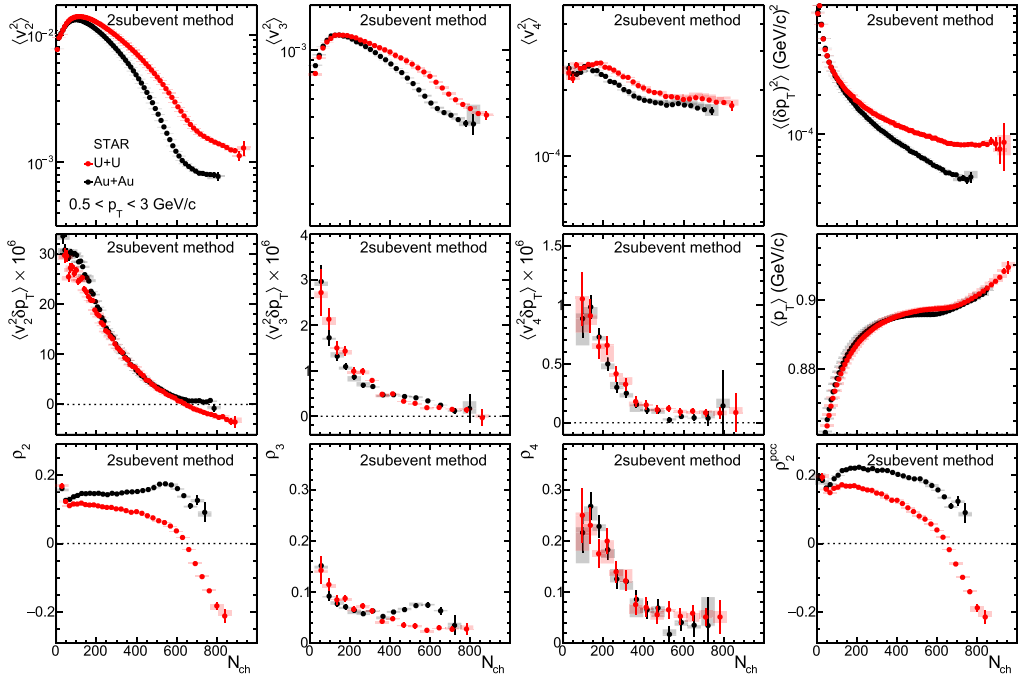


Figure 33. Observables as a function of N_{ch} in U+U and Au+Au collisions for charged hadrons in $0.5 < p_T < 3 \text{ GeV c}^{-1}$.

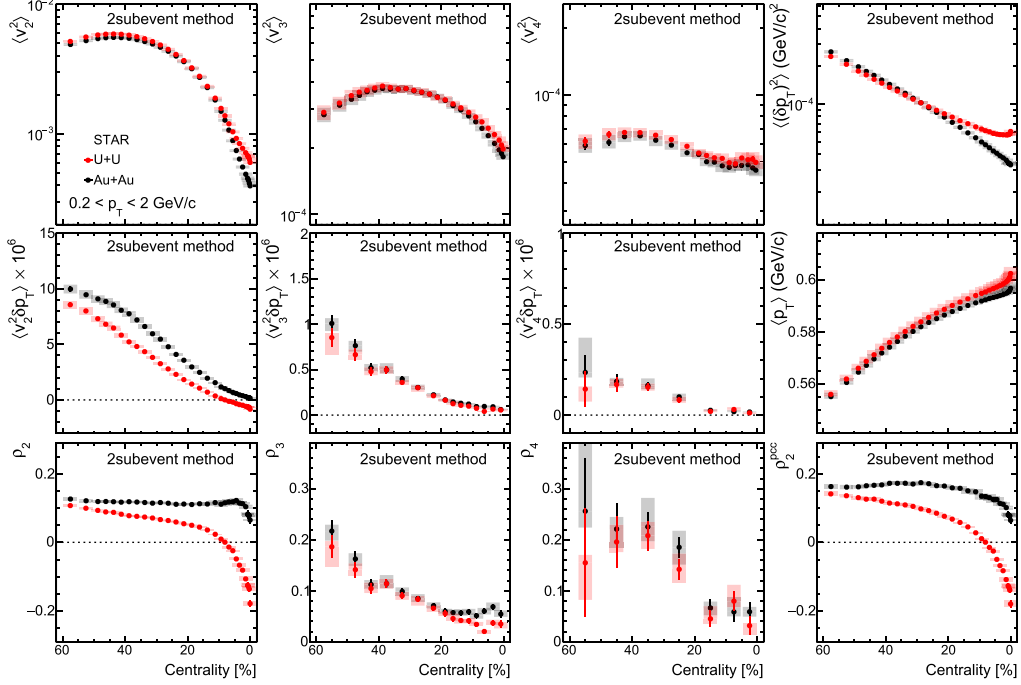


Figure 34. Observables as a function of centrality in U+U and Au+Au collisions for charged hadrons in $0.2 < p_T < 2 \text{ GeV} c^{-1}$.

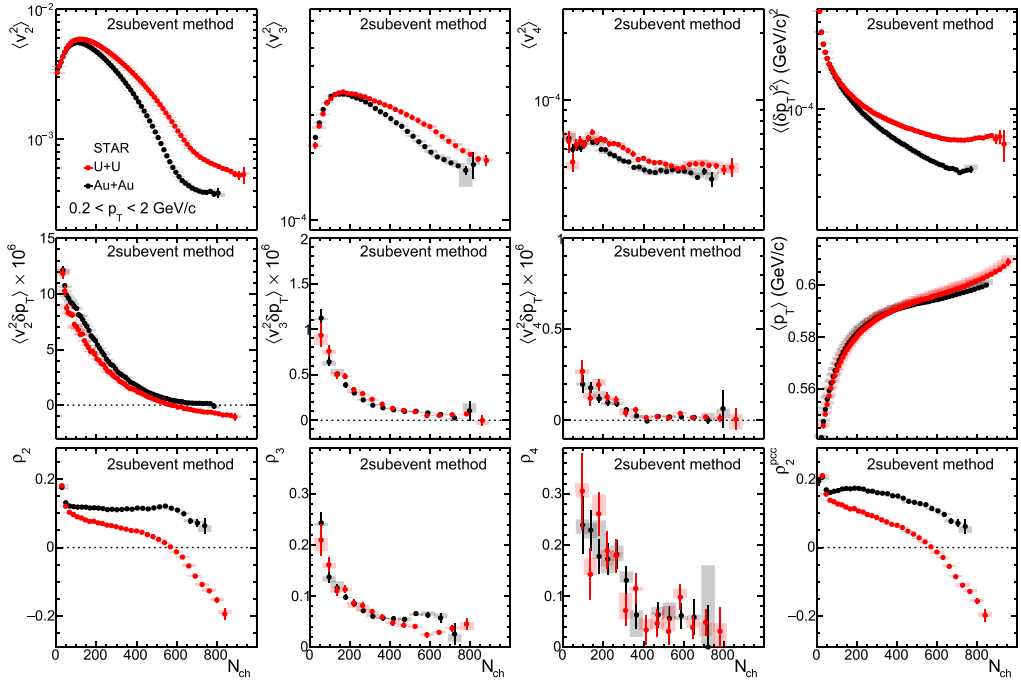


Figure 35. Observables as a function of N_{ch} in U+U and Au+Au collisions for charged hadrons in $0.2 < p_T < 2 \text{ GeV} c^{-1}$.

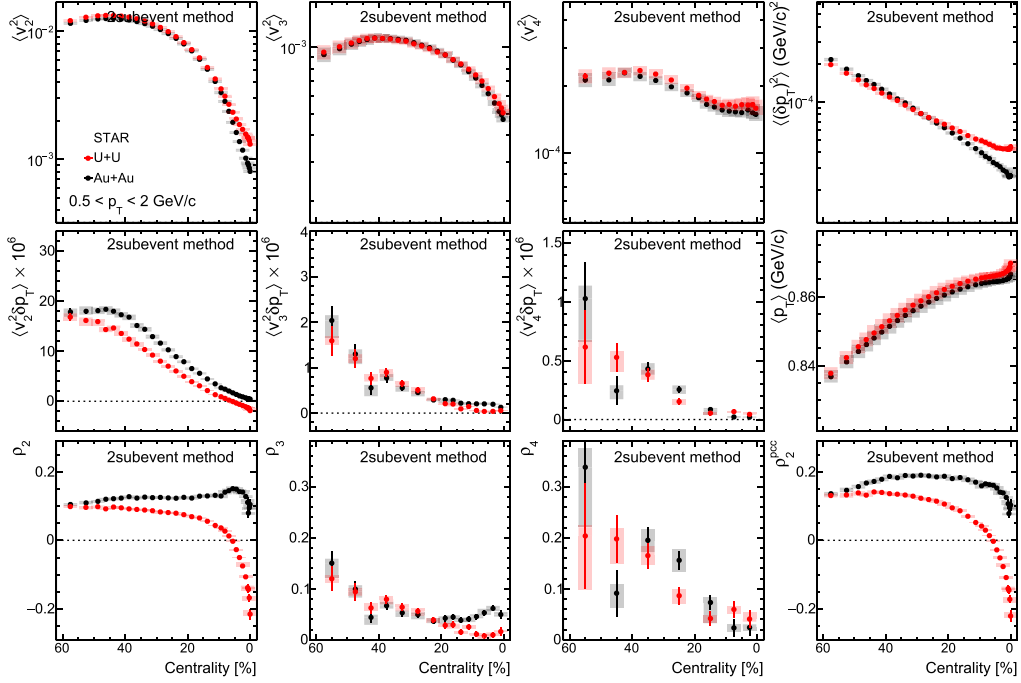


Figure 36. Observables as a function of centrality in U+U and Au+Au collisions for charged hadrons in $0.5 < p_T < 2$ GeV c^{-1} .

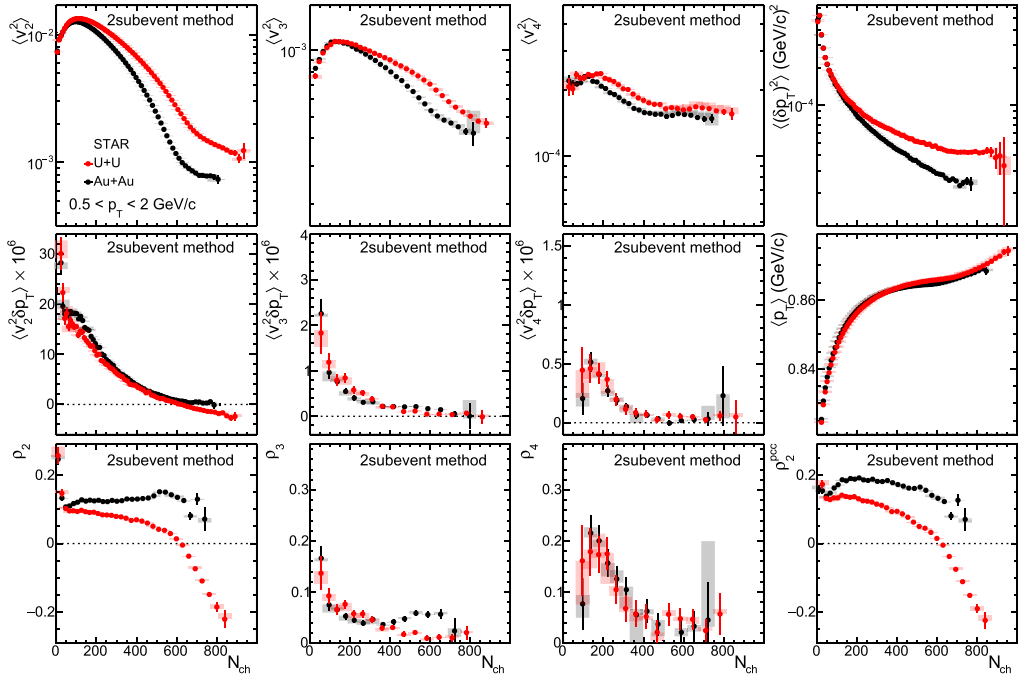


Figure 37. Observables as a function of N_{ch} in U+U and Au+Au collisions for charged hadrons in $0.5 < p_T < 2$ GeV c^{-1} .

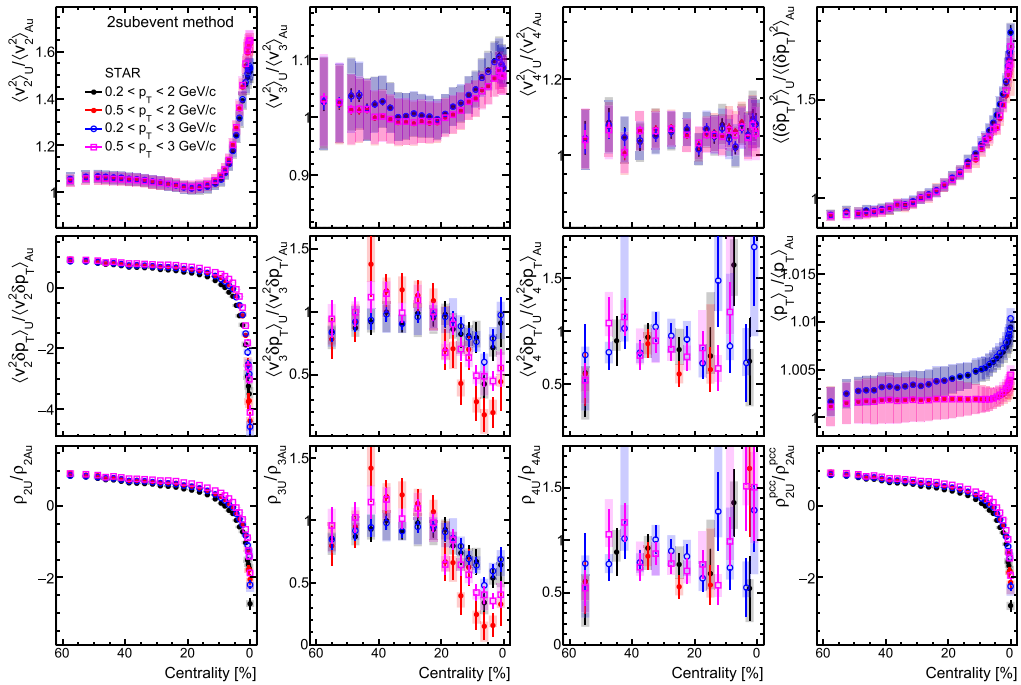


Figure 38. Ratios of observables as a function of centrality for charged hadrons in four p_T ranges.

References

- [1] Busza W, Rajagopal K and van der Schee W 2018 *Annu. Rev. Nucl. Part. Sci.* **68** 339
- [2] Ollitrault J-Y 1992 *Phys. Rev. D* **46** 229
- [3] Ackermann K H *et al* (STAR Collaboration) 2001 *Phys. Rev. Lett.* **86** 402
- [4] Schnedermann E, Sollfrank J and Heinz U W 1993 *Phys. Rev. C* **48** 2462
- [5] Abelev B I *et al* (STAR Collaboration) 2009 *Phys. Rev. C* **79** 034909
- [6] Bernhard J E, Moreland J S, Bass S A, Liu J and Heinz U 2016 *Phys. Rev. C* **94** 024907
- [7] Everett D *et al* (JETSCAPE Collaboration) 2021 *Phys. Rev. C* **103** 054904
- [8] Nijs G, van der Schee W, Gürsoy U and Snellings R 2021 *Phys. Rev. Lett.* **126** 202301
- [9] Luzum M and Petersen H 2014 *J. Phys. G: Nucl. Part. Phys.* **41** 063102
- [10] Jia J 2014 *J. Phys. G: Nucl. Part. Phys.* **41** 124003
- [11] Schenke B, Shen C and Teaney D 2020 *Phys. Rev. C* **102** 034905
- [12] Niemi H, Denicol G S, Holopainen H and Huovinen P 2013 *Phys. Rev. C* **87** 054901
- [13] Bożek P and Broniowski W 2012 *Phys. Rev. C* **85** 044910
- [14] Jia J *et al* 2024 *Nucl. Sci. Tech.* **35** 220
- [15] Jia J 2022 *Phys. Rev. C* **105** 014905
- [16] Abdulhamid M I *et al* (STAR Collaboration) 2024 *Nature* **635** 67
- [17] Abdallah M *et al* (STAR Collaboration) 2022 *Phys. Rev. C* **105** 014901
- [18] Mäntysaari H, Schenke B, Shen C and Zhao W 2024 *Phys. Rev. C* **110** 054913
- [19] Giacalone G, Jia J and Somà V 2021 *Phys. Rev. C* **104** L041903
- [20] Zhang C, Bhatta S and Jia J 2022 *Phys. Rev. C* **106** L031901
- [21] Jia J and Zhang C 2023 *Phys. Rev. C* **107** L021901
- [22] Verney D 2025 *Eur. Phys. J. A* **61** 82
- [23] Cline D 1986 *Annu. Rev. Nucl. Part. Sci.* **36** 683
- [24] Yang X F, Wang S J, Wilkins S G and Garcia Ruiz R F 2023 *Prog. Part. Nucl. Phys.* **129** 104005
- [25] Pritychenko B, Birch M, Singh B and Horoi M 2016 *At. Data Nucl. Data Tables* **107** 1
- [26] Pritychenko B, Birch M, Singh B and Horoi M 2017 *At. Data Nucl. Data Tables* **114** 371–4 (erratum)
- [27] Wu C Y and Cline D 1996 *Phys. Rev. C* **54** 2356
- [28] Moss J M, Terrien Y D, Lombard R M, Brassard C, Loiseaux J M and Resmini F 1971 *Phys. Rev. Lett.* **26** 1488
- [29] Möller P, Sierk A J, Ichikawa T and Sagawa H 2016 *At. Data Nucl. Data Tables* **109–110** 1
- [30] Ryssens W, Giacalone G, Schenke B and Shen C 2023 *Phys. Rev. Lett.* **130** 212302
- [31] Bally B, Giacalone G and Bender M 2023 *Eur. Phys. J. A* **59** 58
- [32] Jia J 2025 *Rep. Prog. Phys.* **88** 092301
- [33] Giacalone G 2020 *Phys. Rev. Lett.* **124** 202301
- [34] Bozek P 2016 *Phys. Rev. C* **93** 044908
- [35] Jia J 2022 *Phys. Rev. C* **105** 044905
- [36] Jia J, Huang S and Zhang C 2022 *Phys. Rev. C* **105** 014906
- [37] Zhang C, Jia J, Chen J, Shen C and Liu L 2025 arXiv:2504.15245 [nucl-th]
- [38] Giacalone G, Schenke B and Shen C 2022 *Phys. Rev. Lett.* **128** 042301
- [39] Giacalone G, Schenke B and Shen C 2020 *Phys. Rev. Lett.* **125** 192301
- [40] Li B-A 2000 *Phys. Rev. C* **61** 021903
- [41] Shuryak E V 2000 *Phys. Rev. C* **61** 034905
- [42] Filip P, Lednický R, Masui H and Xu N 2009 *Phys. Rev. C* **80** 054903
- [43] Shou Q Y, Ma Y G, Sorensen P, Tang A H, Videbæk F and Wang H 2015 *Phys. Lett. B* **749** 215
- [44] Goldschmidt A, Qiu Z, Shen C and Heinz U 2015 *Phys. Rev. C* **92** 044903
- [45] Adamczyk L *et al* (STAR Collaboration) 2015 *Phys. Rev. Lett.* **115** 222301
- [46] ALICE Collaboration 2018 *Phys. Lett. B* **784** 82
- [47] CMS Collaboration 2019 *Phys. Rev. C* **100** 044902

- [47] ATLAS Collaboration 2020 *Phys. Rev. C* **101** 024906
- [48] Fortier N M, Jeon S and Gale C 2025 *Phys. Rev. C* **111** 014901
- [49] Fortier N M, Jeon S and Gale C 2025 *Phys. Rev. C* **111** L011901
- [50] Anderson M *et al* 2003 *Nucl. Instrum. Methods Phys. Res. A* **499** 659
- [51] Llope W J *et al* 2004 *Nucl. Instrum. Methods Phys. Res. A* **522** 252
- [52] Bieser F S *et al* 2003 *Nucl. Instrum. Methods Phys. Res. A* **499** 766
- [53] Llope W J (STAR Collaboration) 2012 *Nucl. Instrum. Methods Phys. Res. A* **661** S110
- [54] Chen J *et al* 2024 *Nucl. Sci. Tech.* **35** 214
- [55] Abelev B I *et al* (STAR Collaboration) 2010 *Phys. Rev. C* **81** 024911
- [56] Adamczyk L *et al* (STAR Collaboration) 2012 *Phys. Rev. C* **86** 054908
- [57] Jia J, Zhou M and Trzupek A 2017 *Phys. Rev. C* **96** 034906
- [58] ATLAS Collaboration 2018 *Phys. Rev. C* **97** 024904
- [59] ATLAS Collaboration 2019 *Phys. Lett. B* **789** 444
- [60] ATLAS Collaboration 2023 *Phys. Rev. C* **107** 054910
- [61] Borghini N, Dinh P M and Ollitrault J-Y 2001 *Phys. Rev. C* **63** 054906
- [62] Mazeliauskas A and Teaney D 2016 *Phys. Rev. C* **93** 024913
- [63] CMS Collaboration 2013 *Phys. Lett. B* **724** 213
- [64] ALICE Collaboration 2013 *Phys. Lett. B* **726** 164
- [65] ATLAS Collaboration 2014 *Phys. Rev. C* **90** 044906
- [66] Adare A *et al* (PHENIX Collaboration) 2013 *Phys. Rev. Lett.* **111** 212301
- [67] Abdulhamid M I *et al* (STAR Collaboration) 2023 *Phys. Rev. Lett.* **130** 242301
- [68] Selyuzhenkov I and Voloshin S 2008 *Phys. Rev. C* **77** 034904
- [69] Lin Z-W, Ko C M, Li B-A, Zhang B and Pal S 2005 *Phys. Rev. C* **72** 064901
- [70] Gardim F G, Giacalone G and Ollitrault J-Y 2020 *Phys. Lett. B* **809** 135749
- [71] CMS Collaboration 2024 *Rep. Prog. Phys.* **87** 077801
- [72] ATLAS Collaboration 2024 *Phys. Rev. Lett.* **133** 252301
- [73] Giacalone G 2020 *Phys. Rev. C* **102** 024901
- [74] Jia J, Giacalone G and Zhang C 2023 *Phys. Rev. Lett.* **131** 022301
- [75] Bozek P and Mehrabpour H 2020 *Phys. Rev. C* **101** 064902
- [76] Loizides C 2016 *Phys. Rev. C* **94** 024914
- [77] Schenke B, Shen C and Tribedy P 2020 *Phys. Rev. C* **102** 044905
- [78] Noronha-Hostler J, Yan L, Gardim F G and Ollitrault J-Y 2016 *Phys. Rev. C* **93** 014909
- [79] Jia J, Huang S, Zhang C and Bhatta S 2024 arXiv:2408.15006 [nucl-th]
- [80] Xu H-J, Zhao J and Wang F 2024 *Phys. Rev. Lett.* **132** 262301
- [81] Löbner K, Vetter M and Hönig V 1970 *At. Data Nucl. Data Tables* **7** 495
- [82] Giacalone G, Nijs G and van der Schee W 2023 *Phys. Rev. Lett.* **131** 202302
- [83] Dobaczewski J, Gade A, Godbey K, Janssens R V F and Nazarewicz W 2025 arXiv:2507.05208 [nucl-th]